Theses and Dissertations

Spring 2012

Graph-based segmentation of the pediatric trachea in MR images to model growth

Richard Lee Amendola
University of Iowa

GRAPH-BASED SEGMENTATION OF THE PEDIATRIC TRACHEA IN MR

IMAGES TO MODEL GROWTH

by

Richard Lee Amendola

A thesis submitted in partial fulfillment
of the requirements for the Master of
Science degree in Biomedical Engineering
in the Graduate College of
The University of Iowa

May 2012

Thesis Supervisor: Assistant Professor Deborah Kacmarynski

Graduate College
The University of Iowa
Iowa City, Iowa

CERTIFICATE OF APPROVAL

_____

MASTER'S THESIS

_____

This is to certify that the Master's thesis of

Richard Lee Amendola

has been approved by the Examining Committee
for the thesis requirement for the Master of Science
degree in Biomedical Engineering at the May 2012 graduation.

Thesis Committee: _____
                   Deborah Kacmarynski, Thesis Supervisor

                   _____
                   Joseph Reinhardt

                   _____
                   Edwin Dove

ACKNOWLEDGMENTS

First of all, I would like to thank my thesis supervisors, Drs. Joseph Reinhardt and Deborah Kacmarynski for their guidance and encouragement over the past two years. It has been a pleasure working with them and this experience is sure to guide my future career decisions. I would also like to thank Dr. Edwin Dove for his perspective and advice on this thesis and Dr. Yutaka Sato for assistance collecting patient images and knowledge in Radiology.

I would like to thank Kang Li and Dr. Milan Sonka for access to the OptimalNet Library for Surface Segmentation. Without this, my research would not have progressed as far as it did. Also, I would like to acknowledge the other graduate students in the lab. I am very fortunate to have the opportunity to work with such great people.

Finally, I would like to thank my parents, family and friends. They have provided me with unwavering love and support throughout my life, especially during the past two years.

ABSTRACT

The upper airways are a major site of congenital and acquired pediatric airway obstruction which is associated with a significant rate of morbidity and mortality. The simplest approach to provide a stable airway is to perform a tracheotomy but it requires complex care with its own complications. Other surgical procedures to reconstruct the obstructed airway require significant expertise. The long-term goal of this project is to develop a greater understanding of congenital abnormalities of the larynx and trachea. The objective of this thesis is to create a process to automatically segment and characterize the pediatric trachea through various measures from magnetic resonance (MR) images. A custom program utilizing a graph algorithm to find the optimal boundary was designed to perform all the desired measurements. This customized measurement tool was optimized utilizing a control cohort of adult patients with 3-dimensional computed tomography (3D CT) scans in addition to MR imaging. When this program was used to measure a pediatric population, it showed a significant correlation between cross-sectional area and age or height of the individual.

TABLE OF CONTENTS

v

LIST OF TABLES

LIST OF FIGURES

viii

ix

CHAPTER 1

INTRODUCTION

Congenital airway abnormalities are usually mild in severity, often presenting with stridor in the first year of life. However, symptoms may worsen with increased activity, development of an airway tract infection or the existence of multiple anomalies. [1] Many times, treatment of these children is challenging because the relative impact of each abnormality is unknown. The simplest approach to provide a stable airway is to perform a tracheotomy but it requires complex care with its own complications. [2-7] Other surgical procedures to reconstruct the airway require detailed knowledge of the normal pediatric airway and its variance between individuals. [8-15] Establishing the characteristics of the normal airway and congenital abnormalities is imperative to quantitatively assess if a reconstructed airway is enlarged enough to provide sufficient airflow.

1.1 Anatomy

The upper airways extend from the nose to the end of the trachea passing through the pharynx, larynx and vocal folds. The structure and function of this system is a major contributor to the conduction of the air to the lungs. The larynx is located in the anterior neck and anterior to the bodies of cervical vertebrae 3–6. It is about 5 cm in length in men and slightly shorter in women. The laryngeal skeleton is made of nine cartilages connected by various soft tissues. Figure 1 shows a cross-section of the thyroid cartilage. The thyroid cartilage makes up the laryngeal prominence which is commonly referred to as the "Adam's apple". The cricoid cartilage is the only complete ring of cartilage and it connects the larynx to the trachea. The upper half of the trachea is in the neck beginning near the sixth cervical vertebra (C6). The lower half lies in the superior mediastinum ending around the fourth or fifth thoracic level of the spine. The trachea is a posteriorly flattened tube and in an adult male, the length of the trachea is approximately 10-11cm,

with an outside diameter of around 2 cm. The anterior and lateral walls are made of alternating incomplete hyaline cartilage rings and soft tissue.
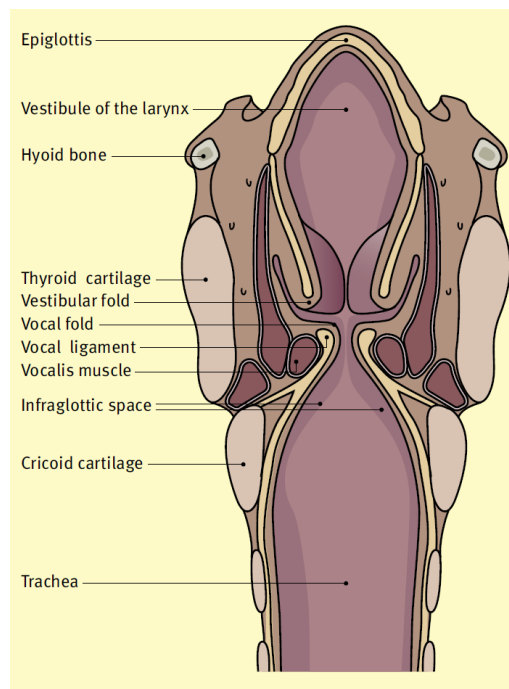
Figure 1. Coronal Section of the Upper Airways [16]

The posterior wall is composed of smooth muscle and fibroelastic tissue. The "C" shape incomplete cartilage rings give the axial cross-section a "D" shape. The soft tissue in the trachea allows for it to expand during deep inspiration and coughing while the incomplete cartilage rings holds its shape. The first, broadest, ring attaches to the cricoid cartilage, while the most distal ring has a triangular lower border forming the carina, an anteroposterior ridge. [16-19] In a newborn, the trachea begins at the level of C4, as a child grows the upper limit of the trachea moves closer to the level of C6. The internal diameter of the trachea is only 3 mm wide at birth, which is small relative to body size.

After it is fully developed it widens to about 15-20mm. [18, 19] In terms of cross-sectional area, the smallest portion of the normal pediatric airway is the cricoid cartilage.
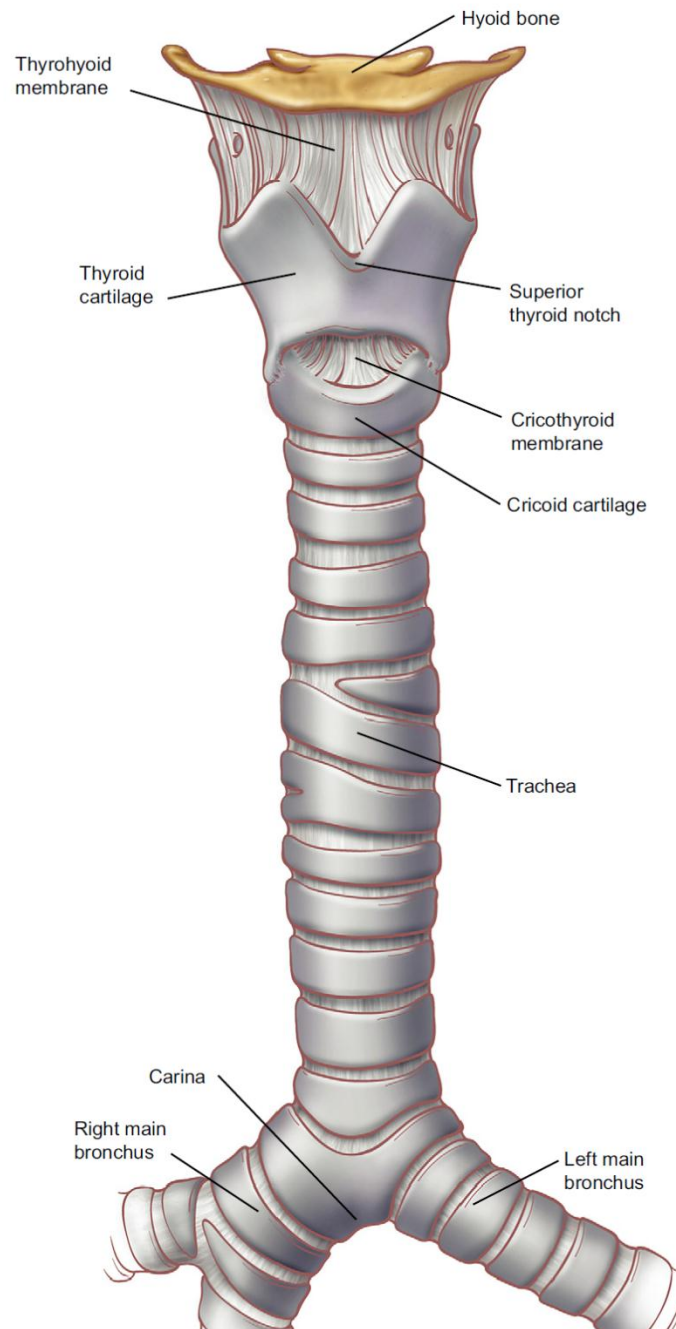
Figure 2. Anatomical Features of the Larynx and Trachea [17]

Since it is at the top of the trachea it provides a significant obstacle to physically measuring the dimensions of the airway below it.

1.2 Clinical Relevance

The upper airways are a major site of pediatric airway obstruction with its accompanying morbidity and mortality. The most common deformity in the larynx is laryngomalacia. This is a congenital condition that involves softening of the tissues in the larynx. This softening causes floppy tissue that can block the airway during inspiration. It is the most common reason for stridor in infants. [1] If laryngomalacia is severe enough, a supraglottoplasty may be performed to reconstruct the soft tissues in the larynx. The appearance of congenital airway abnormalities leading to obstruction often come in different forms and combinations. Many studies have been done to show the prevalence of synchronous airway lesions (SALs) in a pediatric population given one significant airway abnormality. A review in Chicago of children requiring supraglottoplasty due to severe laryngomalacia showed 58% of patients had SALs. Of those, 77% had subglottic stenosis (SGS) and 47% had tracheomalacia, bronchomalacia, or both. 13% of patients required a tracheotomy to stabilize the airway. [20] In another study in Philadelphia performing a review of children requiring hospitalization for their respiratory status, 68% of patients were diagnosed with laryngomalacia, 24% were diagnosed with tracheomalacia and 10% were diagnosed with subglottic or tracheal stenosis. In 37%, multiple airway anomalies were present. Of these, 19% required tracheotomy for management of recurrent respiratory decompensation. [21] In both of these studies, the severity of these conditions is shown by the high number of tracheotomies performed. The relative significance of each airway anomaly is unknown which makes for a complex diagnosis. What to treat and how to treat it are choices made on a case-by-case basis by an experienced interdisciplinary team. [9]

A tracheotomy is a surgery that is performed to bypass airway obstructions in or above the trachea. An incision is made in the anterior of the neck and trachea where a tube is inserted to allow the patient to breathe. Eventually, when the airway is stable, the tube is removed (decannulation). Although a tracheotomy is the simplest approach to a sustainable airway and if performed by an experienced surgeon can be a relatively low risk procedure, it has the potential for life threatening complications especially in infants. A review of infants requiring tracheotomy at Vanderbilt University showed that there were complications at many stages of the procedure. Before attempting decannulation, 50% of the infants developed some kind of complication. The overall rate of patients successfully decannulated was 34%. Among those, the complication rate was 57%. They only experienced one tracheotomy related death out of 127 patients. In older children the complication rate has been shown to decrease. [3] A study in Turkey analyzing the indications for and outcomes of pediatric tracheotomies of children under 16 years of age found that 19% of patients have some kind of complication after surgery with the most common being intervention due to suprastomal granulation tissue. Although there was only a 1% mortality rate from tracheotomy-related issues, a 19% mortality rate was observed due to disease progression or complications. [5] A similar study in New Zealand showed a complication rate as high as 51% for the same population. [4] Even if a child has a successful tracheotomy, there is a significant burden that is placed on the family or caregiver. [2, 6]

Other surgical techniques to repair laryngotracheal abnormalities have been developed. Laryngomalacia has been successfully treated by supraglottoplasty to remove extra, obstructive laryngeal tissue. This procedure has a high success rate and rarely leads to recurrent symptoms or complications. [22, 23] To repair glottis and subglottic stenosis, carefully shaped pieces of the child's own rib are used to open up the airway. This is referred to as laryngotracheal reconstruction. Cricotracheal resection is a procedure also performed to treat subglottic stenosis. It involves removal of the cricoid cartilage and

then the trachea is sewn to the remaining portion of the larynx. [14, 24] If the abnormality is below the larynx, there are more challenging techniques to treat tracheal stenosis. Tracheal stenosis comes in many different forms. Some types can be handled endoscopically with a balloon dilation sometimes assisted with computed tomography (CT) imaging. [15] Other times, an open tracheoplasty is performed. The trachea is cut open and remodeled to achieve the normal dimensions of a trachea. [8-10, 13] During a tracheoplasty, the child is sometimes under cardio-pulmonary bypass. Shortening the time of the procedure would improve outcomes. [11] Treatment of pediatric airway disorders would benefit greatly if more were known about the normal airway including its variation between individuals during growth. The National Institutes of Health has acknowledged identifying the biological and structural components limiting airflow in congenital or acquired disorders of the pediatric upper airway as a priority as well. [25] This enhanced understanding could lead to better diagnosis and insight before surgery as to how much an airway should be enlarged.

The main objective of our research is to characterize congenital and acquired airway abnormalities of the larynx and trachea and try to describe how they impact pediatric airway function.

1.3 Previous Methods of Measuring Airways

Many methods of obtaining the dimensions of a pediatric airway are being developed and used. CT can produce high-resolution images of the airways but are not the best choice for prospectively imaging normal children because of the radiation exposure risks. [26] Intra-operatively, surgeons can measure the size of the smallest part of the airway by comparing it to the outside diameter of an endotracheal tube. Although simple and reproducible, this is only useful for measuring the cross-section of the smallest part of the airway which is usually the subglottic region. It does not provide any information about the rest of the airway. To optimize airflow through the tube, the largest

size that safely fits is used. There is potential to injure the subglottic tissue. The scar tissue can then cause stenosis. [27] Because of this, focus has been shifted to more innovative non-invasive techniques which include: computer analysis of video-bronchoscopy, optical coherence tomography and intraluminal fiberoptic probes. All three of these have shown to have potential to accurately measure pediatric airways in research settings and may be available at those institutions for clinical use but are not widely accessible. [28-32] Common imaging techniques like ultrasound and magnetic resonance (MR) imaging have also been used. Ultrasound imaging has not produced viable results. [31] MR has been used to study the abnormalities that lead to obstructive sleep apnea syndrome (OSAS) in children. A group in Philadelphia successfully quantified the total upper airway volume and cross-sectional area at expected sites of restriction in the nasopharyngeal and oropharyngeal regions. [33, 34] The use of hyperpolarized Helium-3 is also emerging as a plausible modality to image the airways. Although it has been used to show differences in lung ventilation, it may have limited utility for measuring airway dimensions. [35-37]

1.4 How can CT be used?

The size and growth of the normal pediatric airway is not well defined. When considering the dimensions of the upper airway, in particular the trachea, the ability to measure cross-sectional area and different diameters is most imperative. A study completed in 1986 at Harvard used CT imaging to find the range of tracheal lengths, cross-sectional areas, anterior-posterior and transverse diameters, as well as tracheal volumes in a population of normal children. They compared the measurements with the age of each patient. Patient scans were retrospectively obtained, initially acquired as a search for pulmonary metastases. [38] These results should be expanded on for a more complete characterization of the upper airways. A similar cohort of patients would have to be attained and reviewed to avoid unnecessary radiation exposure. Since that study,

numerous commercially available software tools have been developed for segmenting and measuring airways from CT images. One of which is Pulmonary Workstation developed by VIDA Diagnostics, a University of Iowa based company. It is used in over 35 research sites around the world. The Pulmonary Workstation software provides a bronchoscopic view as well as anatomical landmarks in relation to the CT data for the adult airway. Airways are usually segmented with a type of region growing or fuzzy connected algorithm. The skeleton of the airway is then computed and the image is resampled perpendicular to the centerline. Some approaches, including Tschirren et al, modify the initial segmentation with a graph-based approach to compute an optimal boundary. [39]

1.5 How can MR be used?

MR imaging obviates radiation exposure and would be the modality of choice for a prospective study. There are problems associated with MR as well. MR acquisition is slow and usually requires respiratory-gated imaging, so imaging an uncooperative child is difficult. Also, similar segmentation programs as those for CT are not widely available to measure the airway. Liu et al produced a system using Fuzzy Connectedness to segment the upper airways to aid in finding anatomic risk factors for OSAS. Their approach consisted of three main steps: inhomogeneity correction and standardization of the MR imaging intensity scale, creation of a fuzzy connected segmentation of the airway lumen and finally, a centerline computation to compute proper cross-sectional measurements. [40] Since they were imaging young children, sedation along with a dynamic acquisition was required to obtain images. Sedation has been more concerning to radiologists and anesthesiologists in children with respiratory difficulties. If respiratory difficulties are exacerbated during sedation, the MR suite is not the ideal location for supporting an airway. Nevertheless, they were also able to develop good safety and imaging protocols for future dynamic MR studies of the pediatric larynx and trachea. [34]

1.6 Graph Segmentation

The general idea of the graph-based approach is the formation of a weighted graph G = (V,E) with node set V and arc set E. The nodes in V correspond to image pixels (voxels in 3D) and arcs connect the nodes according to a neighborhood system specific to the application. All the nodes and arcs have a corresponding cost quantifying how likely it is to belong to the object of interest. There have been many algorithms developed to utilize graphs and obtain globally optimum image segmentation. Some include spanning trees, shortest paths and graph cuts. Graph cuts have proved to be the most powerful for image segmentation. [41] Graph-based boundary detection is a proven segmentation approach for intrathoracic airways from CT images. [39] The objective of the method is to identify a globally optimal surface. In the general case, a volumetric dataset can be viewed as a 3D matrix $I(x, y, z)$ and the sought after boundary is similar to that shown in Figure 3(a).

The surface is structured that for every (x, y) column, there is a single corresponding z that is part of the surface.
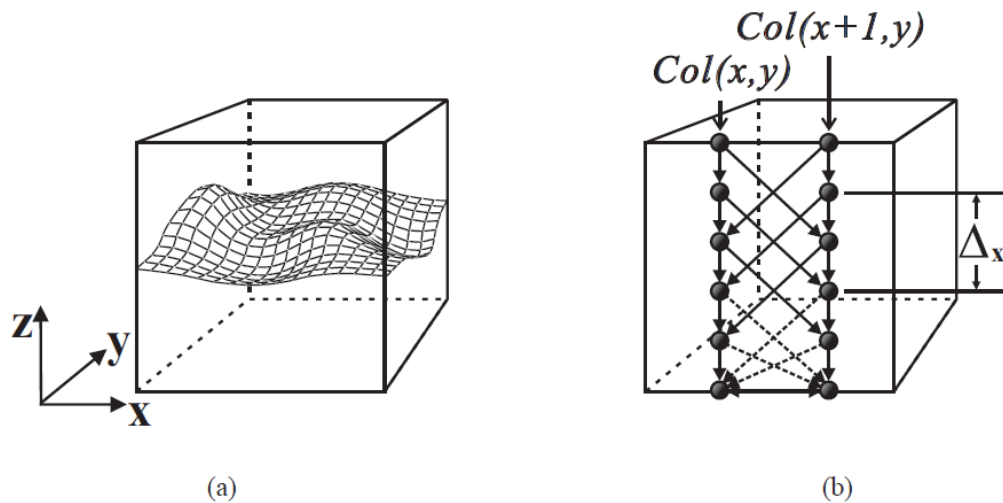
Figure 3. Example of a Valid Surface Segmentation [42]

The total number of voxels included in the surface should be X×Y where X and Y are the sizes of the image in the x and y axes. A potential surface is if it satisfies some application-specific smoothness constraint, defined by two parameters, Δ_x and Δ_y. The smoothness constraint guarantees connectivity of adjacent voxels in the surface. If $I(x, y, z)$ and $I(x + 1, y, z')$ are two voxels on a feasible surface, then $|z - z'| \leq \Delta_x$. Respectively, along the y-axis, if $I(x, y, z)$ and $I(x, y + 1, z')$ are two voxels on a feasible surface, then $|z - z'| \leq \Delta_y$. A small Δ_x or Δ_y corresponds to a stiff surface in the respective axes. Whereas a large Δ_x or Δ_y allows for significant flexibility in the surface. By defining a cost function, a cost value is computed and associated with each voxel of I, denoted $c(x, y, z)$. Generally, the cost value is inversely related to the likelihood that the desired surface would contain the voxel $I(x, y, z)$. An optimal surface is the one with the minimum total sum of voxel costs among all possible surfaces in the image. [41] This optimal surface detection has also been applied to tubular objects. Figure 4, demonstrates the concept of unraveling a tubular object to produce a surface in a similar domain as described above. The tube is resampled radially from the center. [42]

(a)   (b)
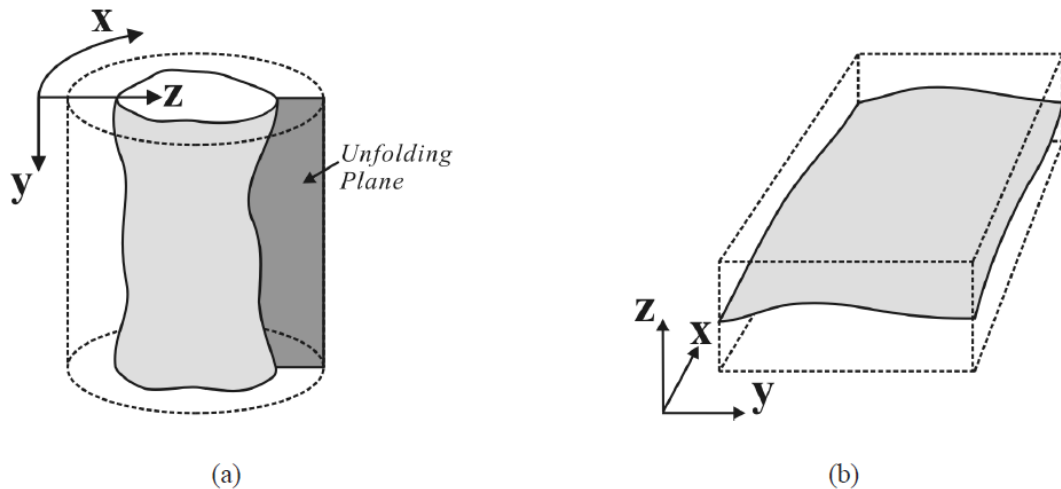
Figure 4. Transformation of a Tube-like Surface to Cylindrical Coordinates. The z-axis is a distance from the center and the x-axis is rotation about the y-axis. [42]

1.7 <u>Modeling Normal Growth</u>

Modeling normal growth of body parts has shown to be a useful approach to predicting the appearance of a disability or disorder later in life. Head circumference is a measure that has been positively correlated with brain volume. [43-45] Microcephaly, in turn, has been related to a higher probability of reduced mental functioning. [46] The Center for Disease Control and Prevention (CDC) produces growth charts for the United States that model height, weight, BMI, and head circumference as children age. Their typical strategy for fitting the data to a model starts with collecting hundreds of normal children's measures. The data is then pooled into age groups and significant percentiles are plotted. The points are then smoothed and fit to an appropriate model. An example of a weight-for-age for boys' growth curve is shown in Figure 5. The CDC uses a variation of polynomial regressions ranging from 3 to 10 parameters depending on which measures they are comparing. [47]

1.8 <u>Our Work</u>

The long-term objective of this project is to develop a greater understanding of congenital abnormalities of the larynx and trachea. It has been shown when there is a severe airway anomaly that requires intervention there is a significant chance of other airway deformities. Assessing the respective impact each anomaly has on the airway is difficult. This is important as many patients require multiple surgeries and a possible tracheotomy if the first procedure is not effective. Some surgeries are performed under cardio-pulmonary bypass so reducing the length of the operation should improve outcomes and lessen the complication rate. By using MR and CT images, a tool can be developed to create a pre-surgical model of a patient's airway. The tool will create a computer model of the airway to analyze air flow. This will assist in defining how each abnormality contributes to the restricted flow. A physical model of the airway will also be constructed. It will be used to let surgeons practice with the diseased airway and plan

how the available tissue should be used to remodel the airway. We hypothesize that this

tool can optimize the initial surgery for these patients.
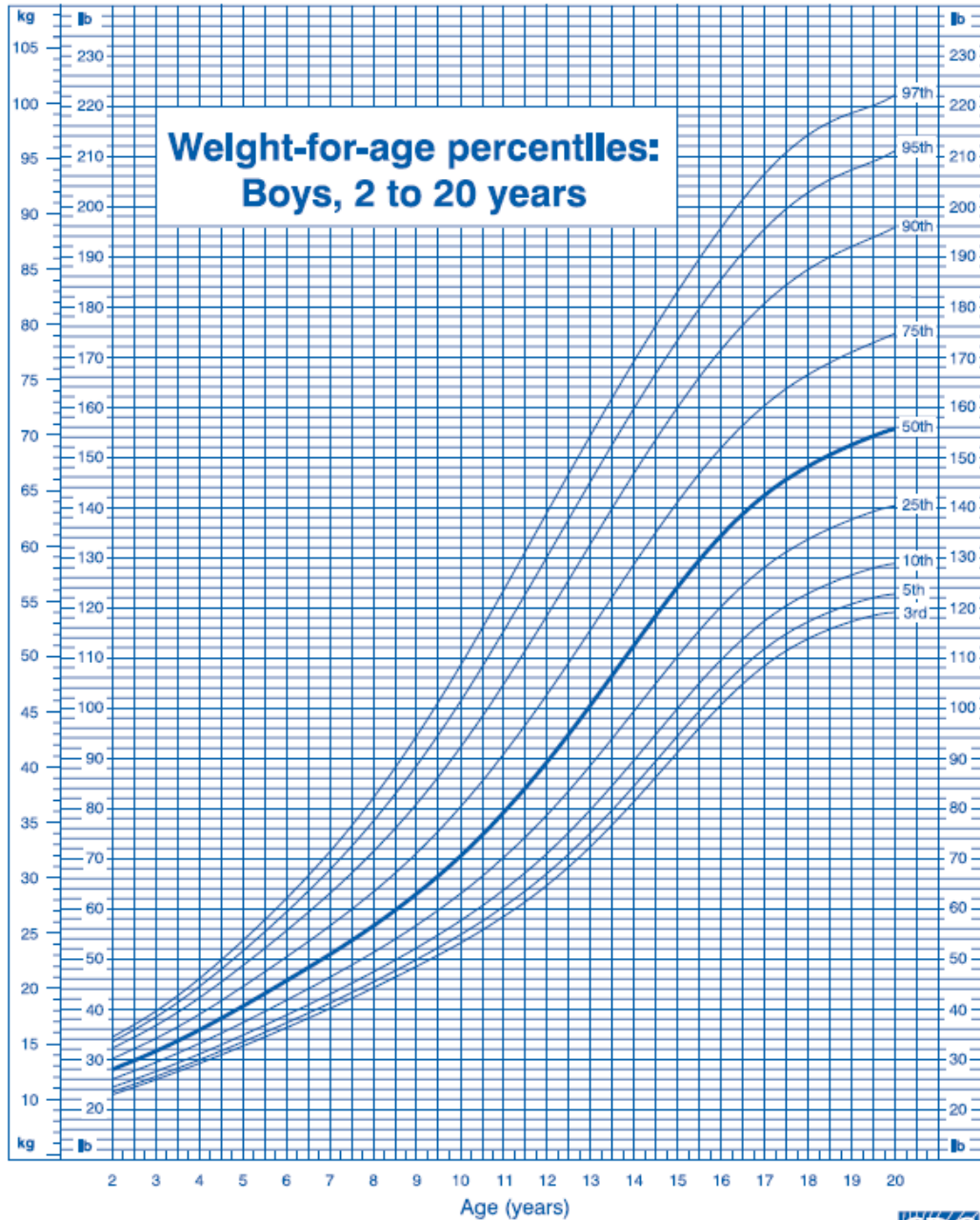
Figure 5. Weight-for-age curve for Boys, 2 to 20 years old. Data provided by the Center for Disease Control and Prevention. [47]

Currently, the best way to perform a prospective study on normal and diseased children is to use MR imaging to characterize the size and shape of the airway. The objective of this thesis is to create a process to automatically segment and measure the pediatric trachea from MR images. The approach we have developed is similar to previous work with CT images. [39, 42] The segmentation tool is implemented as a 3D Slicer module. 3D Slicer is a free, open source software package for visualization and image analysis. It is written in C++ and relies on a variety of toolkits and libraries including VTK, ITK, CMake, Qt and Python. The Insight Toolkit (ITK) contains the majority of image processing filters used in Slicer. The module created for this thesis takes advantage of ITK's filters to perform all of the image processing. Based off seeds points at the vocal cords and carina (manually selected by the user), the program creates an initial segmentation using region growing. It performs a transform to unwrap the image into a cylindrical coordinate system. Then it creates a cost image using the gradients, graylevel and position of voxels in the image to determine which voxels most likely belong to the trachea. Finally, using Boykov-Kolmogorov maximum-flow based algorithm utilizing a forwardstar graph implemented by Li et al, it finds the optimal surface. [42, 48] Using this new segmentation and measuring tool, our objective is to characterize the normal and deformed airway in hopes to correlate the measurements with age, height, weight or BMI. If there are good correlations, these regularly recorded demographics could be used as indicators for how large a child's airway should be.

CHAPTER 2

METHODS

2.1 Retrieving Data

All data was retrospectively collected from the University of Iowa hospitals and clinics. Institutional Review Board approval was received to search for MR and CT images of children and adults with normal airway anatomy. If a patient had images of a normal trachea the deidentified data was printed to a dvd to be analyzed. Patient demographics were recorded for the pediatric population. These included age, weight, height, BMI and gender.

2.2 Description of the Program

The core program built for this thesis work is in C++ language using the Insight Tool-Kit to perform the majority of the image processing. The final product is implemented as a Slicer module but can also be run independently from a command line interface. Figure 6 shows a flow chart of the program.

2.2.1 Initial Segmentation

The objective of the initial segmentation is to highlight voxels that lie in the airway on each slice. The segmentation does not need to be anywhere near perfect, but the centroid of the segmentation on each slice must lie within the airway. In order to create an initial segmentation, the user must select two points to define the upper and lower limits of the airway to be segmented. Slicer allows the selection of Fiducial points. Figure 7 shows the example of points in Slicer. If the image contains the whole airway, the top point should be placed close to the vocal cords and the bottom point close to the carina. Both points must be selected inside the airway. By means of these points, the program crops the original image one slice above the upper limit and one slice below the lower limit. Using the cropped image data, a confidence connected region growing is performed with the Fiducial points as seeds.
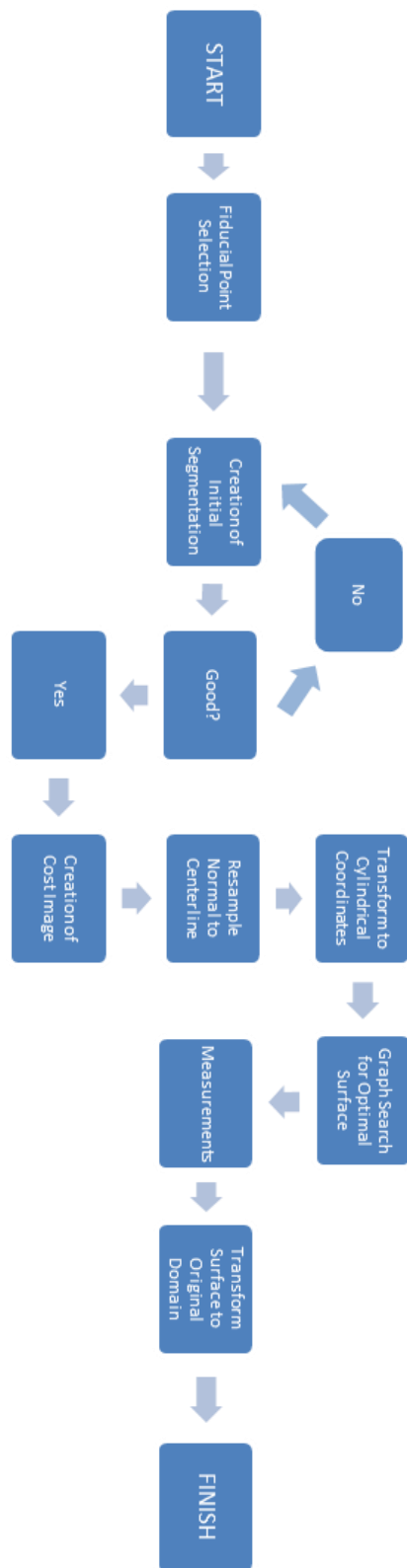
Figure 6. Flow Chart of the Program.
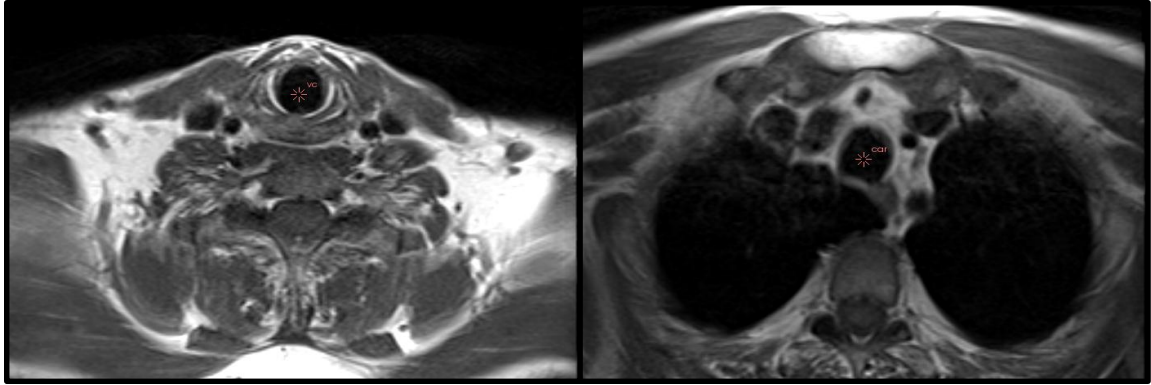
Figure 7. Example of Fiducial Points in 3D Slicer
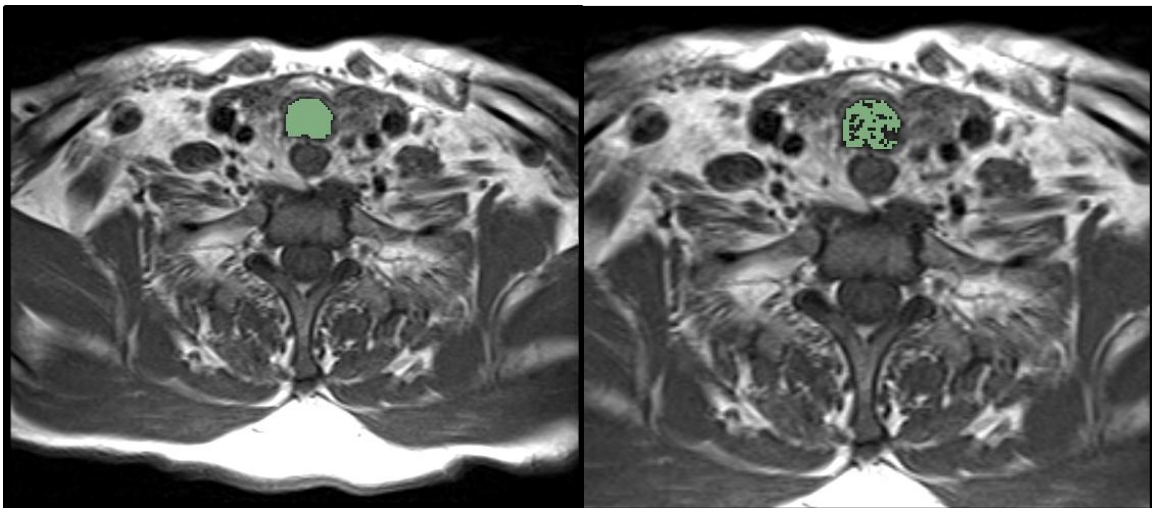
Figure 8. Two Adequate Segmentations to Initialize the Program

By calculating the mean and standard deviation of the Fiducial points and their neighbors, the filter creates a range of values to include in the region growing operation. Once the process is finished it is repeated using the voxels found in the previous region growing to calculate a new mean and standard deviation. Figure 8 shows an example of a two sufficient initial segmentations. Even though the segmentation on the right is not very good, the centroid of the highlighted pixels is within the airway so it is adequate.

The user has the ability to manipulate the parameters to affect the number of iterations and the range of values included until a satisfactory segmentation is reached. If necessary, the user can use the manual tools provided by 3D Slicer to edit the segmentation.

2.2.2 Creation of Cost Image

The creation of a cost image is the most important part of the program. The original image is multiplied by a cost function to obtain the cost image. The lowest valued voxels in the cost image define the voxels that are most likely to belong to the border of the trachea and the airway. The program initially defines the cost image as if the highest valued pixels are most likely to belong to the border and then inverts it. Previous work using CT images has used a combination of the 1st and 2nd derivatives to provide an accurate cost function. [49] Since MR images do not have as strong of a gradient along the border of the airway, two other parameters were added into the cost function to contribute. They included a parameter to consider the value of the voxels in the original image and another parameter to include position of the voxels in the image. The idea behind these parameters is that darker pixels that are closer to the center of the image are more likely to belong to the trachea. Figure 9 is an example of the different images combined to produce the cost image. The final image (D) is actually applied after the image is resampled along the centerline for simplicity and accuracy.

2.2.3 Resample Normal to the Centerline

After the cost image is calculated, it is resampled along the centerline of the airway. There are two main objectives of this step; one is to create an airway that is straight so that it can be unraveled and the other is to transform the trachea to a domain where taking true cross-sectional measurements is simple. True cross-sectional measurements are important because they are the most meaningful, easy to understand and transfer to a clinical setting. The initial segmentation is used to resample.
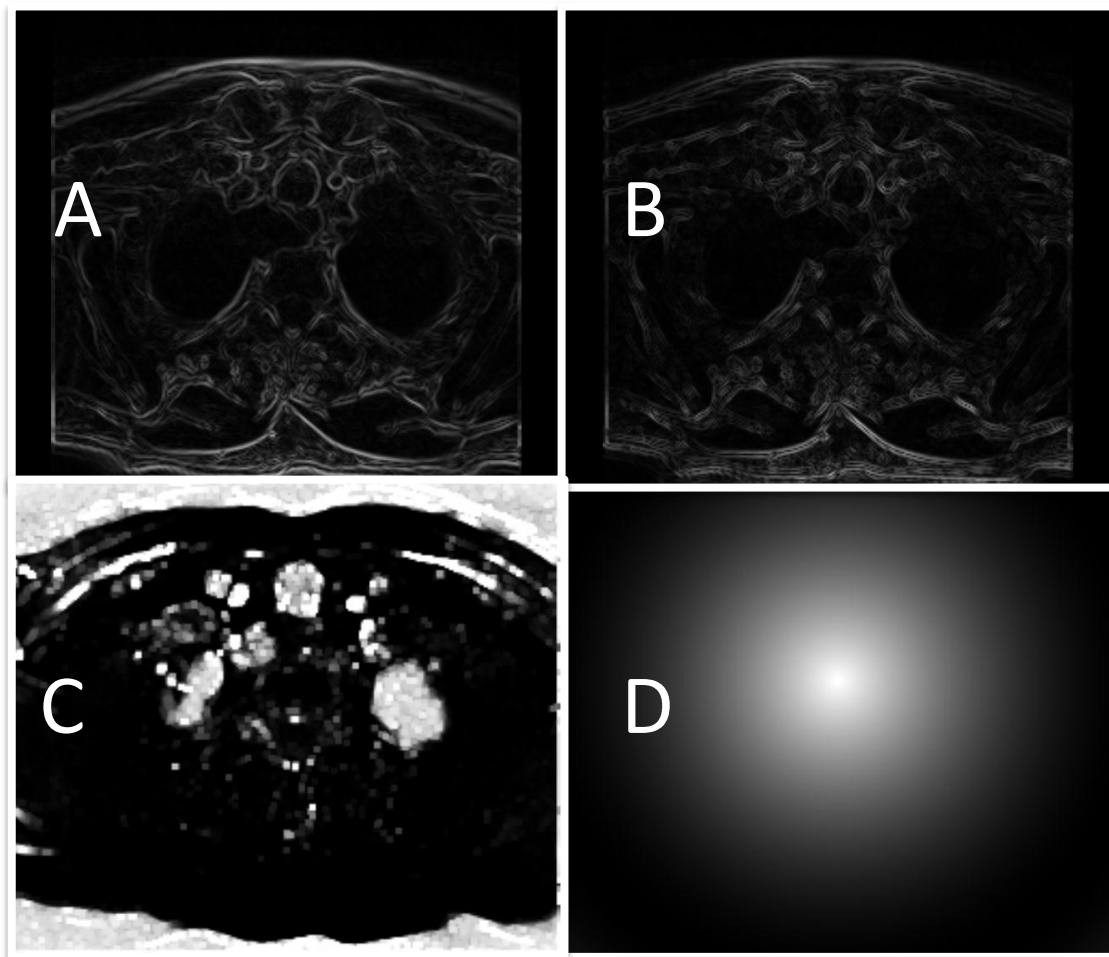
Figure 9. Axial slices of the different components that contribute to the final cost image. A-First Derivative, B-Second Derivative, C-Voxel Value Weighted Image, D-Position Considered Image

For every slice in the initial segmentation, the centroid of the highlighted voxels is calculated. Connecting the centroids, a line is created through the lumen of the trachea. At each slice a new plane is created normal to the centerline and the cost image is resampled producing a new cost image with a straight airway (as shown in Figure 11) in the axial direction. When the image is resampled normal to the centerline, all of the physical coordinates are recorded so the final surface segmentation can be transformed back to the original domain for visualization purposes only. At this point, as stated

before, the position parameter to the cost function (Figure 9 D) is applied and then the cost image is inverted. Figure 10 and 11 show the final cost image.

Figure 10. The final cost image. (a) Cost Image Before Inversion (b) Final Cost Image

Since the trachea is now known to be in the center of the image, the outside portion can be cropped from the image. The program computes the maximum diameter of the initial segmentation and crops the cost image to 120% of that length in both axes of the axial plane.

2.2.4 Transform to Cylindrical Coordinates

For use in the OptimalNet library, the surface of interest must be of the form $z = (x, y)$ ($y = (x, z)$, $x = (z, y)$ respectively). Meaning for every x and y value in the dataset there is only one z value. Currently, at this point in the program, the cost image portrays the trachea as a cylinder. The cost image is now transformed to cylindrical coordinates. This is similar to "unwrapping" the image. In the current domain, x and y coordinates correspond to left-right and anterior-posterior respectively. To transform the data, it is resampled radially from the center of the image.
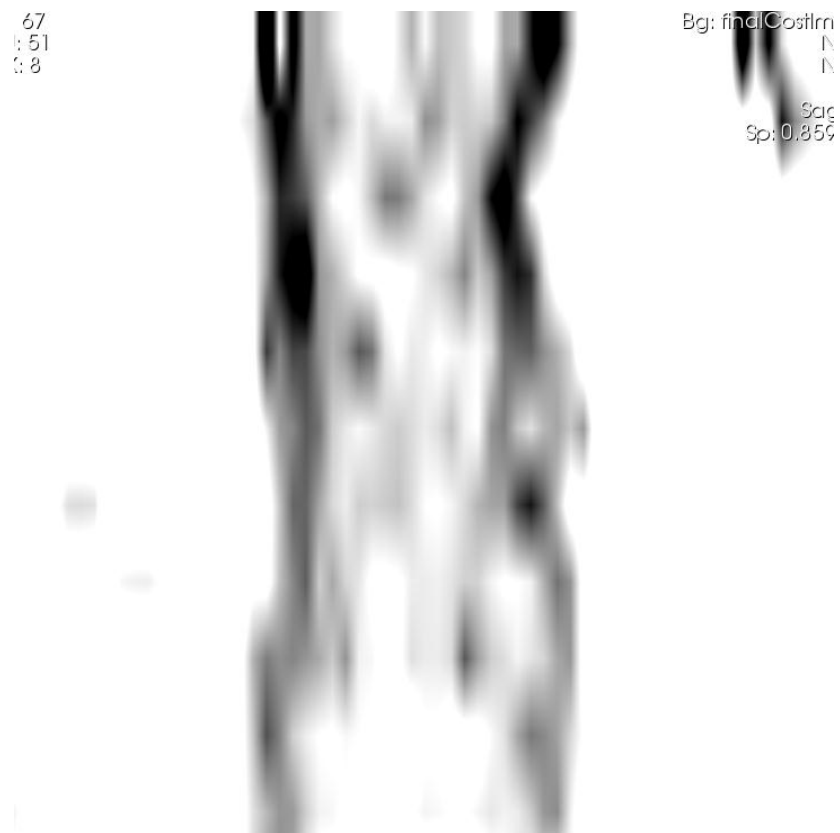
Figure 11. A Screenshot From 3D Slicer of a sagittal slice of the cost image.
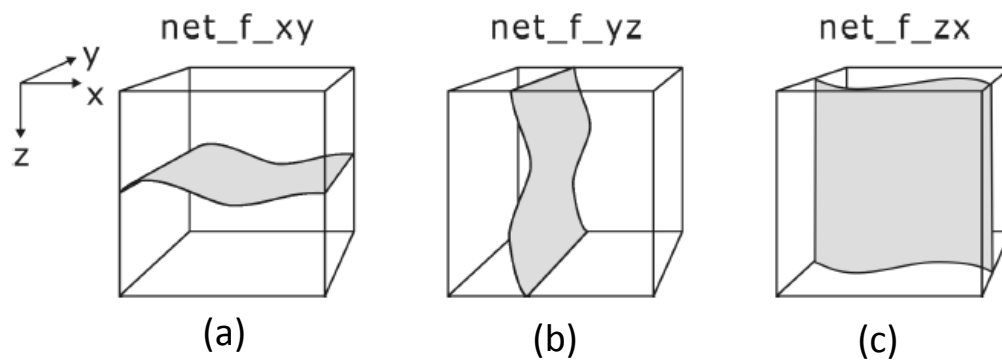
Figure 12. Possible Surface Orientations for the OptimalNet Library. [43]

In the new cylindrical domain, *x* is degrees and *y* is the distance from the center. The lumen is at the top of the airway (close to the center), followed by the trachea and the rest of the tissues. The trachea is now a surface parallel to *z-x* plane, similar to Figure 12 (c).

2.2.5 Graph Search for Least Cost Surface

Now, the trachea is represented as a reasonably flat surface in one plane. Via the OptimalNet library, the Boykov-Kolmogorov maximum-flow based algorithm utilizing a forward-star graph is used to find the least cost surface. The algorithm takes four user defined parameters as input. The first parameter is the orientation of the surface. Figure 12 shows the possible orientations accepted by the OptimalNet library. The next two parameters are the smoothness constraints defined as the largest possible change in the *x* and *z* direction (Δ_x and Δ_y) for adjacent surface voxels. The output is the lowest cost surface in the form of one *y* coordinate for every *x* and *z* pair.
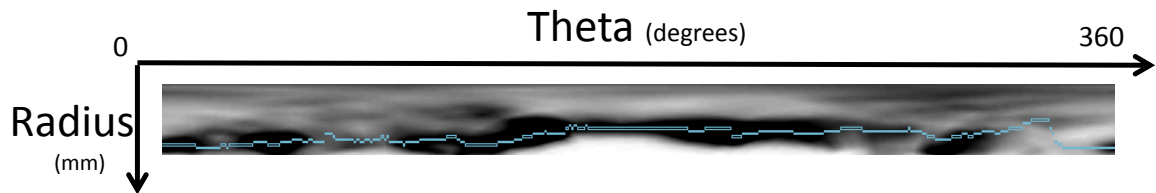
Figure 13. Example of the Optimal, Lowest Cost Surface

The last parameter is to force a circularity constraint. Since each end of the surface in the *x* direction is actually touching in the real-world domain, the algorithm will force the voxels on either ends of the *x*-axis to be within the smoothness constraint. Figure 13 is an example of one axial slice of the optimal surface found by the algorithm.

2.2.6 Measurements

With the surface still in cylindrical space, the maximum, minimum and average diameter as well as perimeter and cross-sectional area are calculated for every slice. All of the measurements except perimeter are calculated without any processing. Since the MR images are acquired at a relatively low resolution, when the image is transformed to cylindrical coordinates by resampling radially 360 times, it ends up over-sampling the image. This over-sampling leads to a surface that is constantly shifting between voxels but not changing very much globally. In turn, the perimeter is over-estimated. Figure 14 depicts this problem. Essentially, (a) and (b) have relatively the same area but the perimeters are drastically different.

(a)   (b)
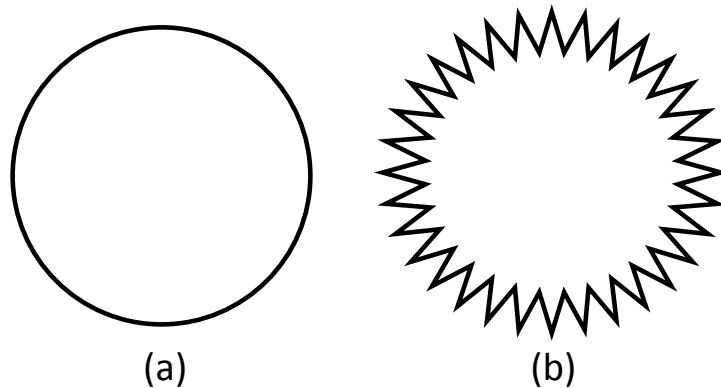
Figure 14. Exaggerated Illustration of the effect of a locally bumpy surface on Perimeter Measurement

To adjust for this when calculating perimeter, each coordinate on the surface is averaged with the adjacent four coordinates to provide a more accurate perimeter calculation.

2.2.7 Surface Transformation to Original Image Domain

For visualization purposes, the surface is transformed back to the original image domain. It does this by first converting it from cylindrical coordinates back to Cartesian coordinates. Since the physical points of the planes normal to the actual trachea were recorded, the mask is then back projected to the original domain. This concludes the description of the software.

2.3 Parameter Optimization

There are five main parameters that affect the surface segmentation produced. Three parameters contribute to the cost function, termed alpha (α), gamma (γ) and beta (β). The cost function is produced by multiplying together three images ranging from 0-1. The first image is a weighted average of the first and second derivatives (I',II') of the original image. The weighting parameter is alpha. Alpha ranges from 0-1 so if it is close to 1, the first derivative is weighted more and if it is close to 0 the second derivative is weighted more. The second image is the invert (negative) of the original image (1-voxelvalue) to the power of gamma. The greater the value of gamma, to more the weight dark pixels in the original image have. The last image is 1 at the center of the image and 0 at the edges of the image. (1-distanceFromCenter) The greater the value of beta, the quicker the fall-off is from 1 to 0. Essentially, the cost function is equation 1.

$$(\alpha I' + (1 - \alpha)I'') * (1 - voxelvalue)^{\gamma} * (1 - distanceFromCenter)^{\beta} \quad \text{Equation 1}$$

Although, the final image, $(1 - distanceFromCenter)^{\beta}$ is not multiplied into the cost function until it is resamples about the centerline of the trachea. Figures 15, 16 and 17 show the effects of manipulating alpha, gamma and beta.
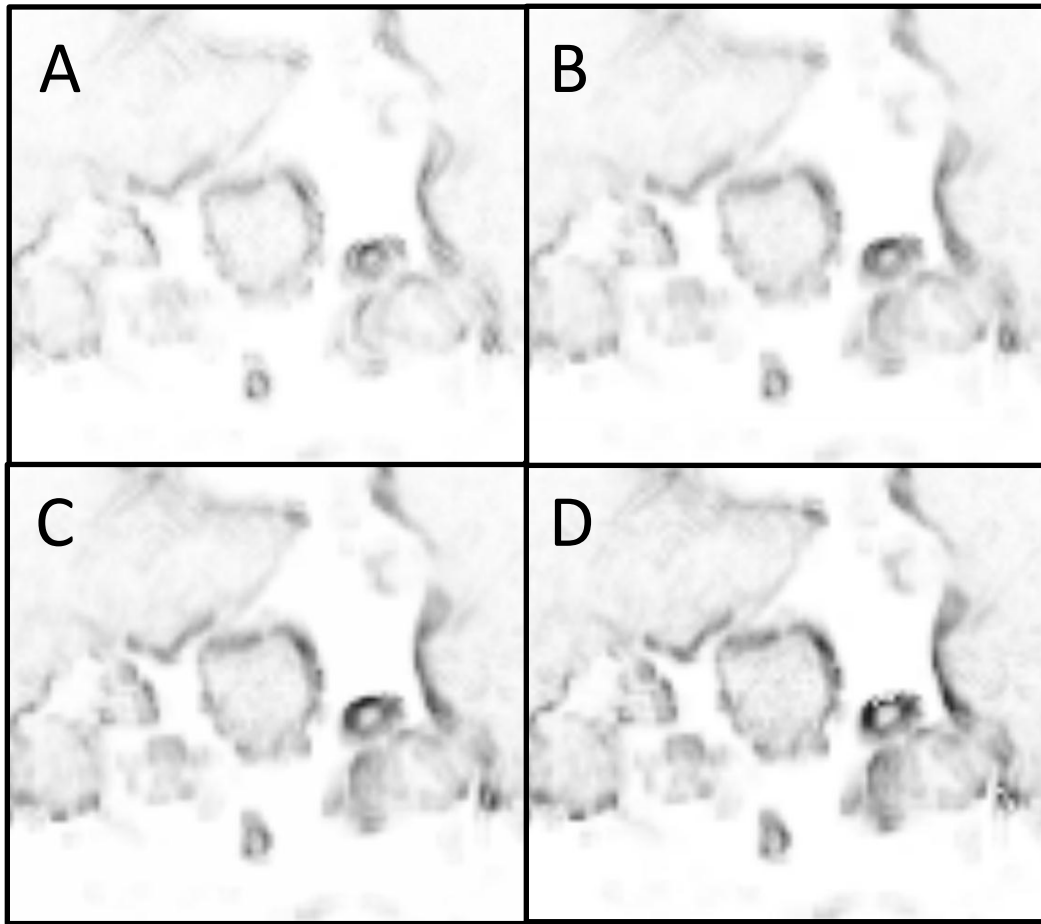
Figure 15. Effects of Changing Alpha. Beta and Gamma are held constant at 0.66 and 5 respectively. In A, alpha is 0; In B, alpha is 0.33; In C, alpha is 0.66; In D, alpha is 1.
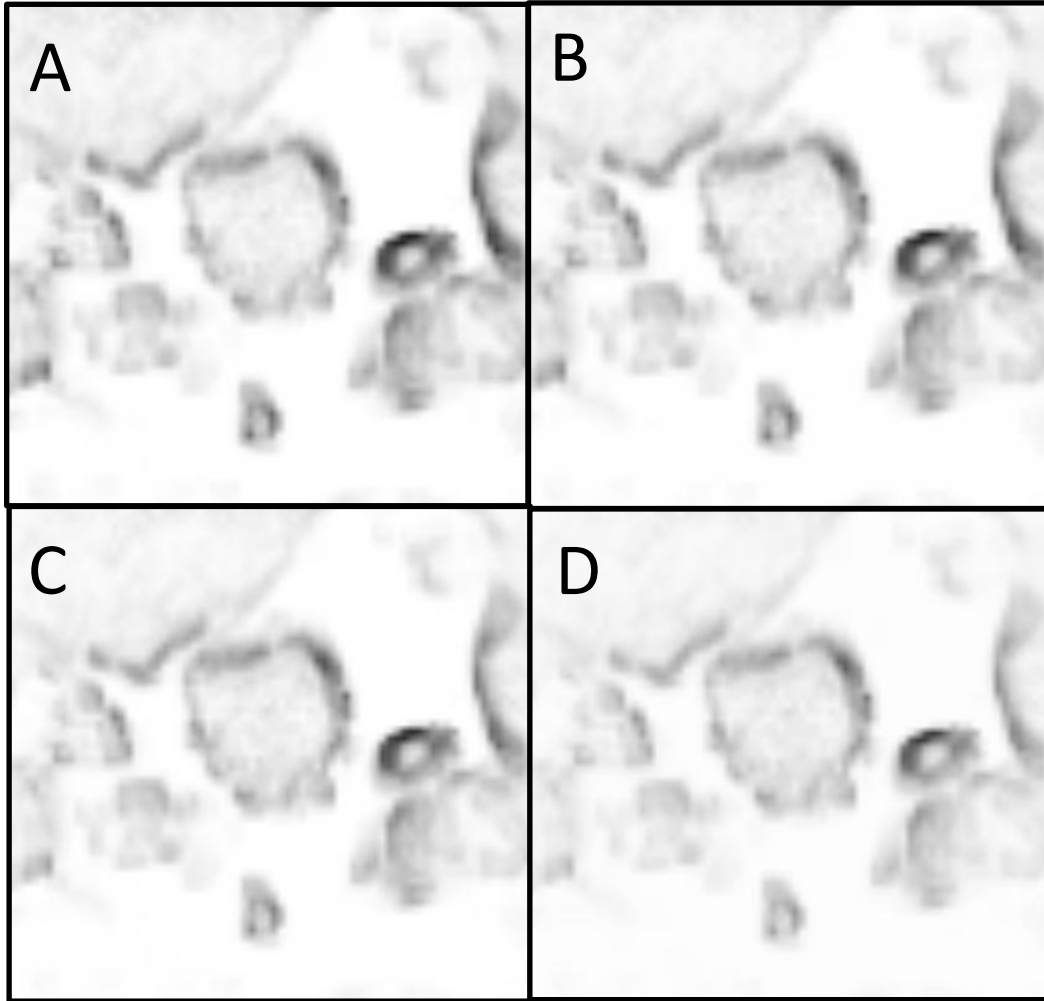
Figure 16. Effects of a Change in Beta. Alpha and Gamma are held constant at 0.66 and 5 respectively. In A, beta is 0; In B, beta is 0.33; In C, beta is 0.66; In D, beta is 1.
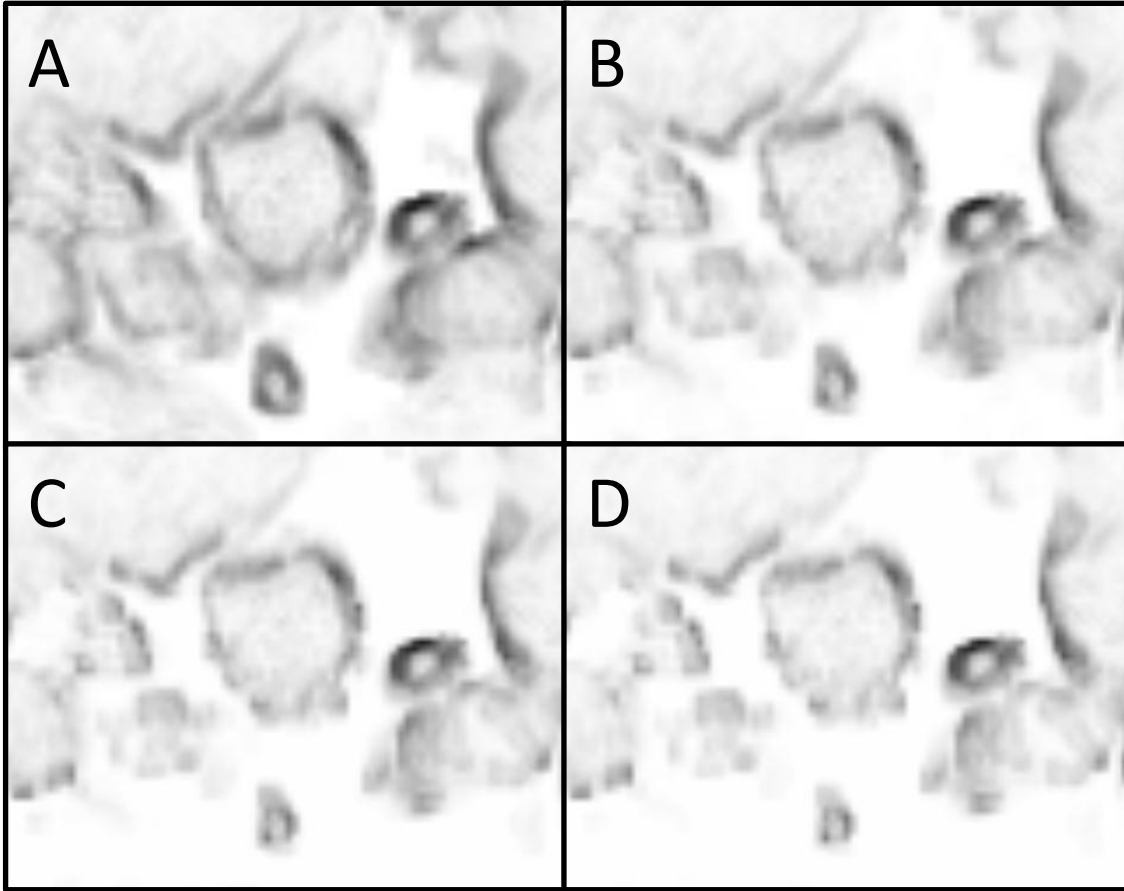
Figure 17. Effects of a Change in Gamma. Alpha and Beta are both held constant at 0.66. In A, gamma is 1; In B, gamma is 3; In C, gamma is 5; In D, gamma is 7.

The last two of the five parameters that affect the final segmentation were described above in the Graph Search for Least Cost Surface. They are termed xSmooth (Δ_x) and zSmooth(Δ_y) and determine the flexibility of the surface.

To optimize the parameters to create the best segmentation, we searched for patients with CT and MR scans of the trachea. The CT scans were measured with Pulmonary Workstation. It is a validated program developed by VIDA Diagnostics that has the capability to segment and measure airways from CT scans. The output from Pulmonary Workstation was used as the optimal solution. Since children are constantly

growing, we were not able to find any pediatric patients with matching CT and MR images of their airways. Instead, we chose to use adult patients because the CT and MR scans could be acquired months or years apart and the trachea should not have experienced significant change in shape or size. Six adult patients were collected. To compare the measurements of the CT and MR scans, the images were registered. Under the assumption that the patient was in a similar position when both the CT and MR images were acquired, 3D Slicer's Fast Rigid-Registration module was used to register the images. This module allows for the "moving" volume to be translated and rotated in all axes with no change in the shape and uses mutual information as the metric. Mutual information allows for comparison of images where the intensity values do not correspond to the same tissues. In order to initialize the algorithm, they were manually aligned. Figure 18 shows example registration results. Once the images were registered, two fiducial points were created to mark the upper and lower most overlapping axial slices of the trachea. Using Pulmonary Workstation, the trachea in the CT scan was analyzed and measurements were recorded for the CT scan at every slice. Since the CT scan was acquired at a much higher resolution, the measurements are interpolated to produce measurements at the same position as the MR slices. Now, the results from our module using the MR image could be directly compared to the Pulmonary Workstation measurements. The comparison metric was the average square difference in cross-sectional area of each slice of the segmentations. To grasp how each parameter effects the MR segmentation a broad search was done over the error space. All combinations for alpha from 0-1 in increments of 0.2; beta from 0-8 in increments of 1; gamma from 0-30 in increments of 2; xSmooth as 1, 2 or 3 and zSmooth as 1 or 2 were tested. The parameter sets were sorted based on each case's own error. The parameter set then received a rank for that case, 1 being the best. The final error for that parameter set is the sum of the ranks across all the cases. This insures the error is equally weighted across cases.
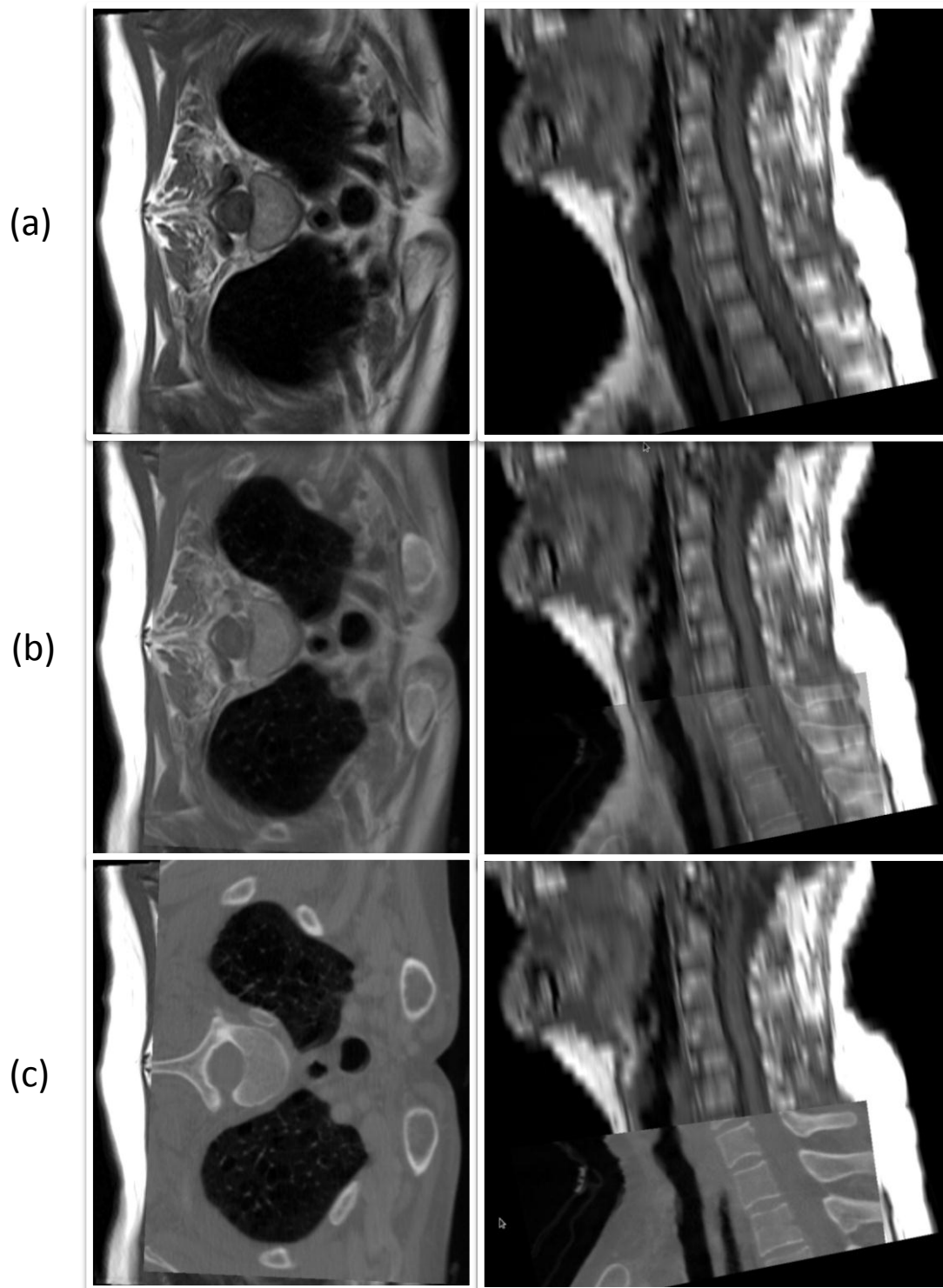
Figure 18. Example of the Rigid Registration of the MR and CT images The left side is a axial slice and the right side is a mid-sagittal slice. (a) The MR image. (c) The CT image overlaid on top of the MR image. (b) The images blended together.

After it could be seen which group of parameter sets led to the lowest error, a more specific test of the error space was conducted. The specific test tried the parameter combinations of alpha from 0.75 to 1 in increments of 0.05; beta from 0 to 4 in increments of 0.25; gamma from 10 to 20 in increments of 0.5;xSmooth and zSmooth were held constant at 2 and 1 respectively.

2.4 Estimation of Error

In order to estimate the error when this program is used to measure tracheal dimensions in the real world, the optimization process was performed on five of the six cases, leaving one out as a test case. It was repeated for all six cases. This was accomplished by using data collected from the initial global search of the error space. The rankings of five cases (instead of six) were summed and sorted based off of this sum. The parameter set with the smallest sum of ranks was used to measure left-out dataset. Minimum and maximum diameter, cross-sectional area and perimeter were plotted for a test case as position from the carina.

2.5 Measuring Pediatric Population

The optimal parameter set settled on during the optimization process with all six datasets was used to measure a pediatric population consisting of 25 individuals. Measurements were averaged over the whole trachea to produce one metric for each patient. The results were plotted against age, weight, height and body mass index. (BMI) An attempt was made to fit a second order polynomial to each plot. These results were compared to Griscom's study that used measurements from CT data. [1]

To validate that the automatic segmentation results of the pediatric trachea are close to what an expert would manually segment, a pediatric otolaryngologist segmented the trachea on five axial slices of every image. Error was measured as the distance between the closest boundary points of the manual and automatic segmentations. Since different results are obtained depending on which segmentation the distance is measured

from, the average is used. Figure 19 depicts this process. The distance from a manual

boundary point to the closest automatic boundary point is measured (1, red line) and then

the closest manual boundary point from that automatic point is measure (2, green line)

and the average of the two is computed.
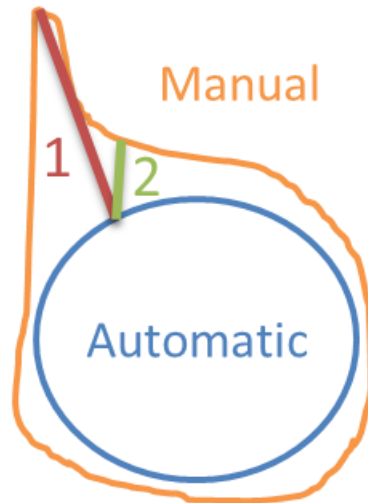
Figure 19. An Example of how the boundary point error is calculated. The blue line is the automatic segmentation and the orange line is the manual segmentation. An average of the red and green lines is used as the error for that manual point.

CHAPTER 3

RESULTS

3.1 <u>Parameter Optimization</u>

Using the measurements of corresponding CT datasets analyzed with VIDA's

Pulmonary Workstation as the gold standard, the cost function parameters alpha, beta and

gamma as well as the smoothness constraints xSmooth and zSmooth were optimized to

produce the same results. Initially, a global search of the error space was conducted by

trying many possible combinations of the parameters. In Table 1, the 20 best parameter

sets are shown with their corresponding rank for each case as well as the sum of the

ranks. Theoretically, the best possible parameter set for these six patients would have a

sum of ranks of 6.

Table 1. The best 20 parameter sets from the initial broad, global search of the error
space.

alpha	beta	gamma	xSmooth	zSmooth	Patient 1	Patient 2	Patient 3	Patient 4	Patient 5	Patient 6	Sum Of Ranks
0.8	2	14	2	1	444	1737	148	461	768	383	3941
1	2	14	2	1	432	1331	393	170	1774	84	4184
1	2	14	3	1	433	1317	409	169	1700	194	4222
0.8	2	14	3	1	459	1724	381	460	786	413	4223
0.8	0	22	2	1	112	347	268	515	1661	1443	4346
1	1	18	3	1	325	1060	503	188	1669	608	4353
1	3	12	3	1	675	1747	210	205	1365	177	4379
0.8	3	10	3	1	625	1624	341	429	1258	132	4409
0.8	2	12	2	1	412	1339	494	422	1629	115	4411
0.8	2	12	3	1	434	1319	518	398	1626	124	4419
0.8	3	10	2	1	631	1688	340	444	1221	125	4449
1	2	16	3	1	474	1673	259	212	1390	460	4468
0.8	1	22	3	1	320	635	76	669	1102	1696	4498
1	0	20	1	1	134	620	593	283	2190	694	4514
0.8	2	16	2	1	507	1696	101	549	702	991	4546
0.8	3	8	3	1	508	1324	530	337	1710	142	4551
1	1	20	2	1	337	1070	279	266	1679	933	4564
0.8	1	14	3	1	236	1208	848	359	1659	259	4569
1	2	16	2	1	455	1685	207	238	1556	432	4573

Columns alpha through zSmooth are the values for each parameter in that given
parameter set. Columns Patient 1 through Patient 6 are the ranks that parameter
set received for that patient. (1 being the best and 5184 being the worst) The last
column is the sum of the individual ranks. It is from this rank that the parameter
sets are sorted.

Using Matlab, surface plots representing the error for different parameter sets were created. Figures 20 through 25 show beta and gamma plotted against each other for different combinations of alpha, xSmooth and zSmooth. All of the colorbars represent the same scale and can be compared directly. When xSmooth is changed from 1 to 3 in figures 20 through 22, it produces a dark blue area in both figures 21 and 22. When xSmooth is 3 there is a quicker slide to a large error than when xSmooth is 2. Figure 23 shows there is a clear disadvantage to changing zSmooth to 2 as opposed to 1. Figures 24 and 25 show how a lower alpha increases the overall error and shrinks the dark blue area.

Figure 20. A surface plot of the error space when beta and gamma are changing and alpha, xSmooth and zSmooth are held constant. Alpha is 1, xSmooth is 1 and zSmooth is 1. Dark blue squares represent parameter sets that produce the best results and dark red are parameter sets that produce the worst results. The units on the color bar are the sum of ranks. (the last column in table 1)

Figure 21. A surface plot of the error space when beta and gamma are changing and alpha, xSmooth and zSmooth are held constant. Alpha is 1, xSmooth is 2 and zSmooth is 1. The pink square will be referenced during the more specific optimization in the next section. (Figures 26 through 31)

Figure 22. A surface plot of the error space when beta and gamma are changing and alpha, xSmooth and zSmooth are held constant. Alpha is 1, xSmooth is 3 and zSmooth is 1.

Figure 23. A surface plot of the error space when beta and gamma are changing and alpha, xSmooth and zSmooth are held constant. Alpha is 1, xSmooth is 2 and zSmooth is 2.

Figure 24. A surface plot of the error space when beta and gamma are changing and alpha, xSmooth and zSmooth are held constant. Alpha is 0.8, xSmooth is 2 and zSmooth is 1.

Figure 25. A surface plot of the error space when beta and gamma are changing and alpha, xSmooth and zSmooth are held constant. Alpha is 0.6, xSmooth is 2 and zSmooth is 1.

It can be seen that good results are most dependent on alpha, beta, gamma and zSmooth. Holding xSmooth at 2 and zSmooth at 1, more specific parameter combinations of alpha ranging from 0.75 to 1, beta from 0 to 4 and gamma from 10 to 20 were tested. Table 2 shows the 20 best parameter sets in this more specific range. Figures 26 through 30 show the effects of gamma and beta with a constant alpha, xSmooth and zSmooth. Essentially, the next set of figures is a blown-up view of the pink box in Figure 21. All of the color bars represent the same scale, but are different from the color bars in figures 19 to 24. As alpha increases in figures 26 to 31 the dark blue area increases. In figure 30, when alpha is 0.95, the dark blue area is the largest.

Table 2. The best 20 parameter sets following a more specific search of the error space.

alpha	beta	gamma	xSmooth	zSmooth	Patient 1	Patient 2	Patient 3	Patient 4	Patient 5	Patient 6	Sum Of Rank
0.95	1.75	15	2	1	868	925	470	471	1239	203	4176
1	2.5	13	2	1	1316	1062	420	228	1181	12	4219
0.95	2.25	13	2	1	1082	932	590	341	1278	14	4237
0.95	2	14	2	1	995	903	756	327	1249	13	4243
1	2	14	2	1	1040	895	710	157	1441	78	4321
0.95	2.5	12.5	2	1	1250	972	531	328	1226	28	4335
0.95	1.75	14	2	1	920	856	1006	181	1366	18	4347
0.95	2.25	12.5	2	1	1131	893	565	267	1394	103	4353
0.95	3	11.5	2	1	1414	1084	559	269	932	111	4369
0.95	1.75	13.5	2	1	879	892	929	201	1396	88	4385
1	2.5	12.5	2	1	1296	930	534	138	1403	115	4416
0.95	0.75	19.5	2	1	558	309	395	409	1345	1402	4418
0.95	2.75	13.5	2	1	1400	1209	709	525	594	6	4443
1	1.75	14	2	1	984	835	892	190	1505	59	4465
0.95	2.25	13.5	2	1	1072	976	598	566	1147	121	4480
0.95	2.5	12	2	1	1301	931	579	232	1294	164	4501
0.9	3.25	11	2	1	1458	1199	483	700	558	114	4512
1	2.25	13	2	1	1076	933	872	161	1380	94	4516
0.95	2.75	12.5	2	1	1335	1082	637	497	912	61	4524

Columns alpha through zSmooth are the values for each parameter in that given parameter set. Columns Patient 1 through Patient 6 are the ranks that parameter set received for that patient. (1 being the best and 2142 being the worst) The last column is the sum of the individual ranks. It is from this rank that the parameter sets are sorted.
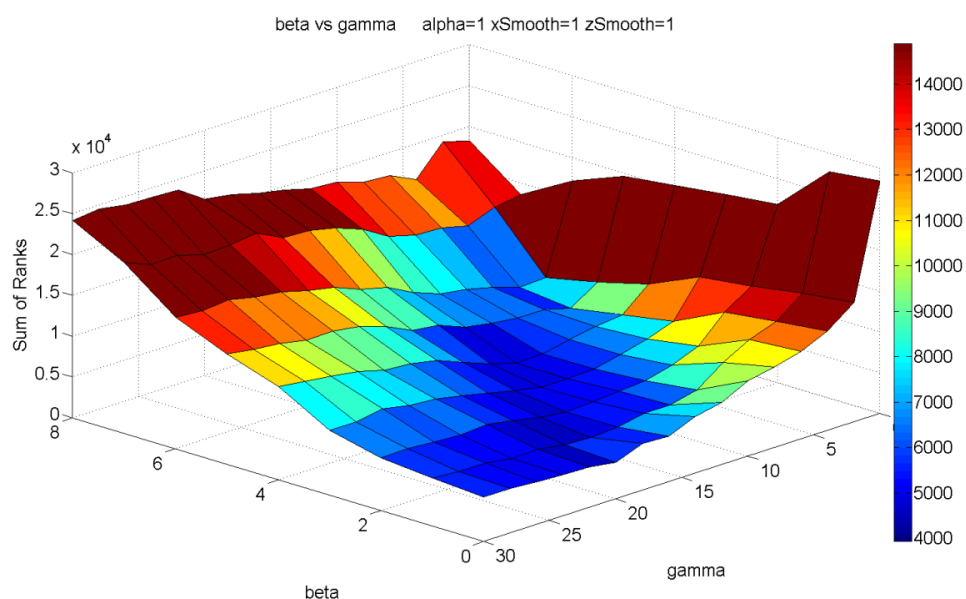
Figure 26. A surface plot of the error space when beta and gamma are changing and alpha, xSmooth and zSmooth are held constant. Alpha is 0.75, xSmooth is 2 and zSmooth is 1. Dark blue squares represent parameter sets that produce the best results and dark red are parameter sets that produce the worst results. The units on the color bar are the sum of ranks. (the last column in table 2)
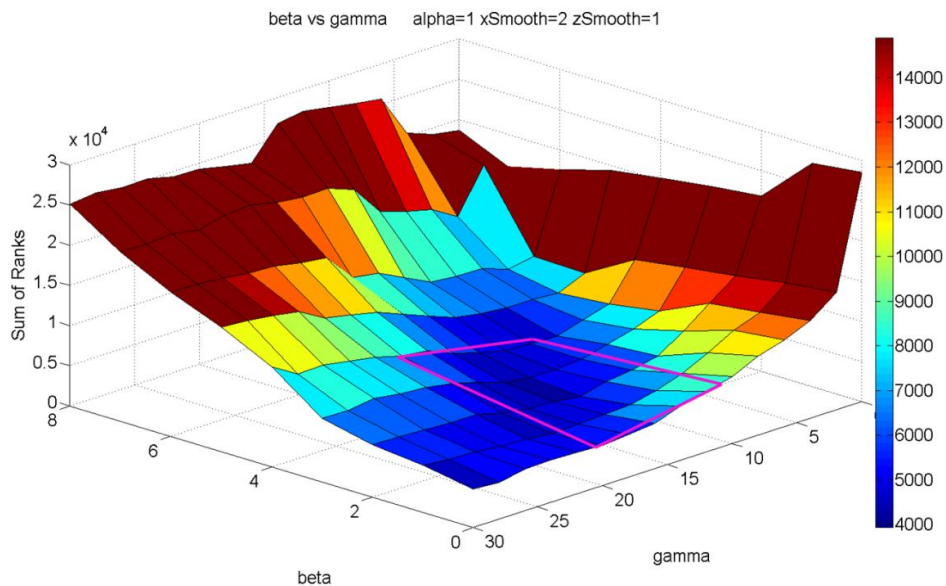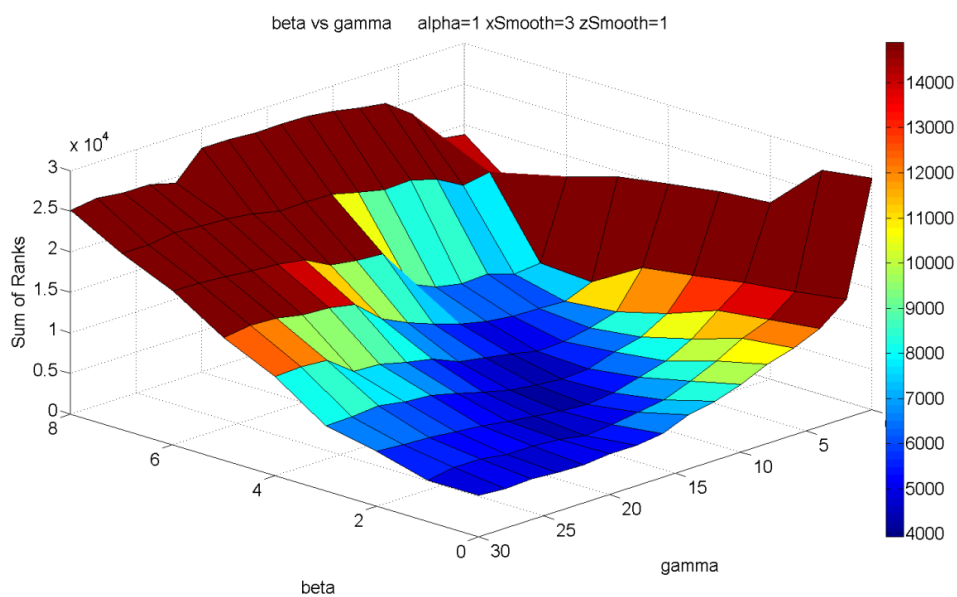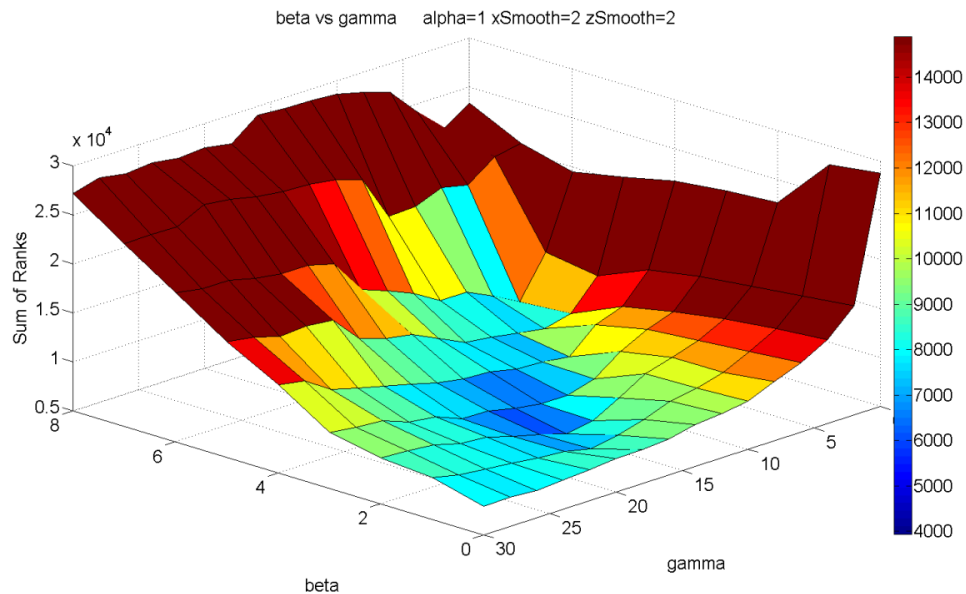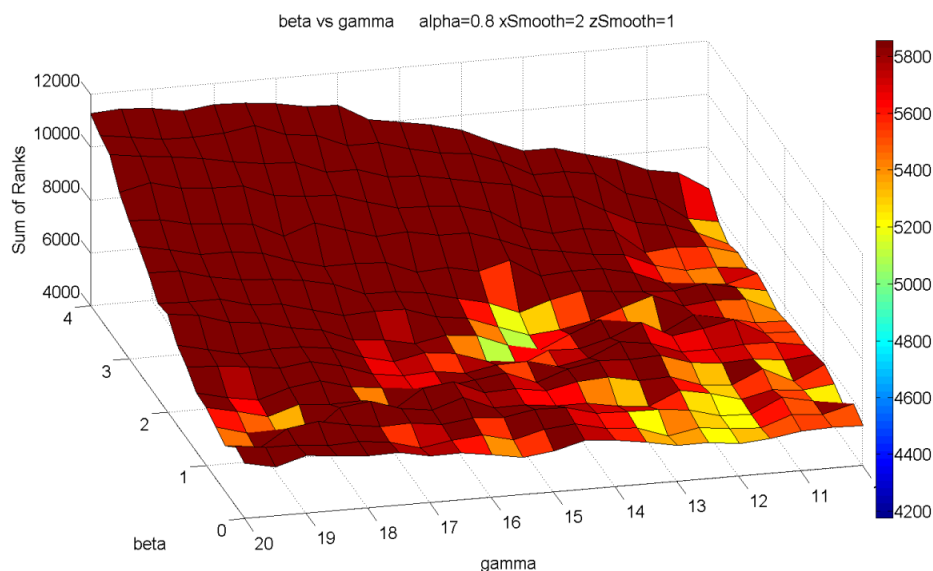

Figure 27. A surface plot of the error space when beta and gamma are changing and alpha, xSmooth and zSmooth are held constant. Alpha is 0.8, xSmooth is 2 and zSmooth is 1.
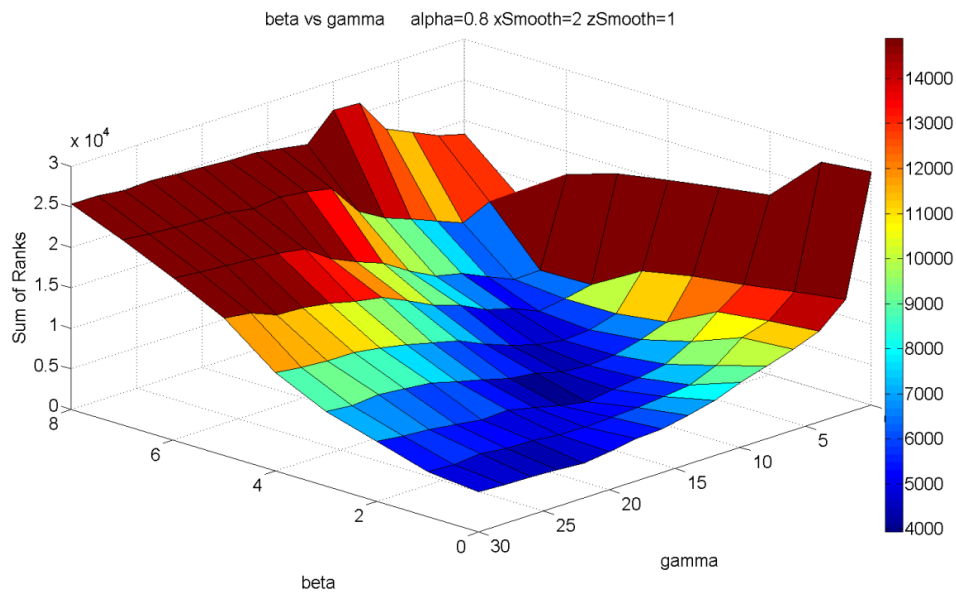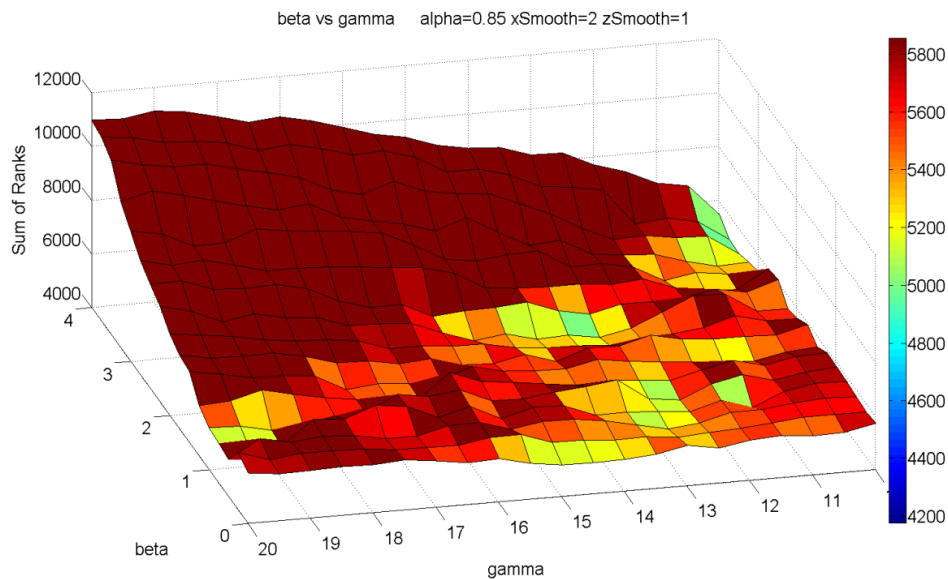
Figure 28. A surface plot of the error space when beta and gamma are changing and alpha, xSmooth and zSmooth are held constant. Alpha is 0.85, xSmooth is 2 and zSmooth is 1.
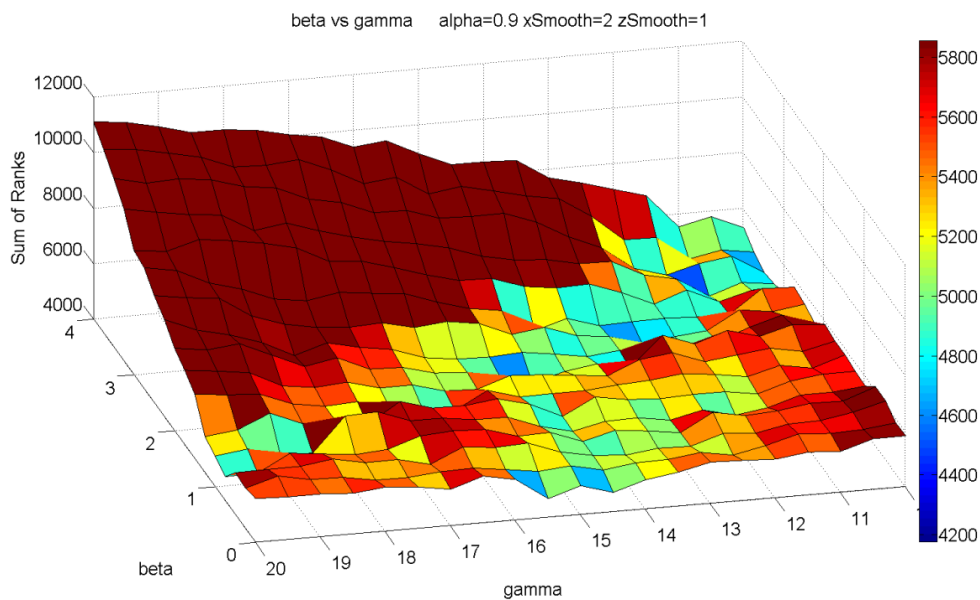
Figure 29. A surface plot of the error space when beta and gamma are changing and alpha, xSmooth and zSmooth are held constant. Alpha is 0.9, xSmooth is 2 and zSmooth is 1.
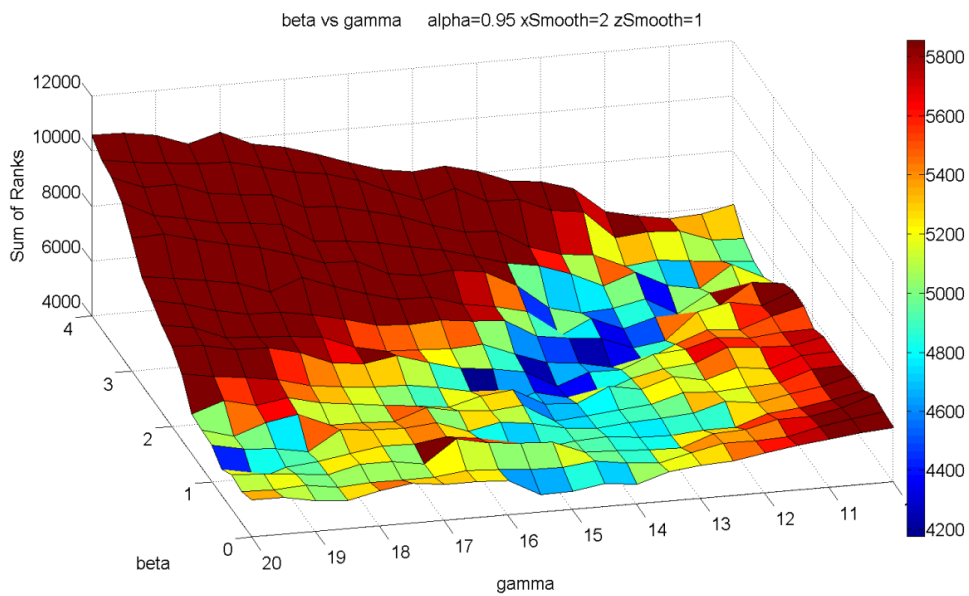
Figure 30. A surface plot of the error space when beta and gamma are changing and alpha, xSmooth and zSmooth are held constant. Alpha is 0.95, xSmooth is 2 and zSmooth is 1.
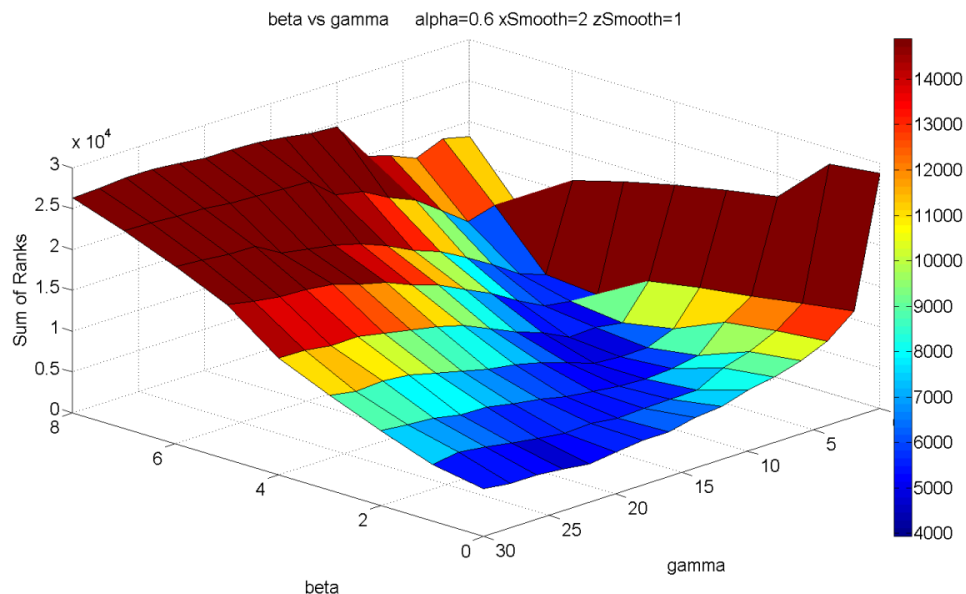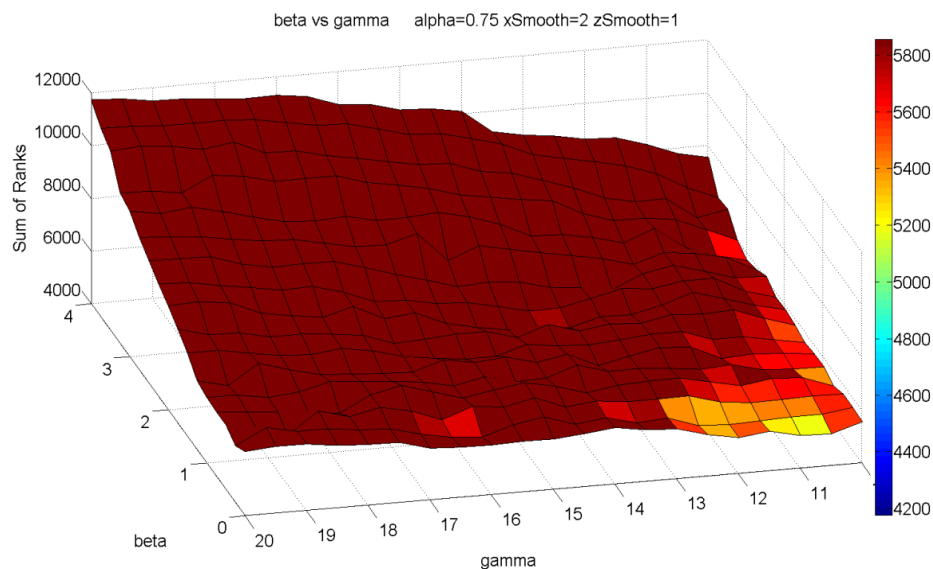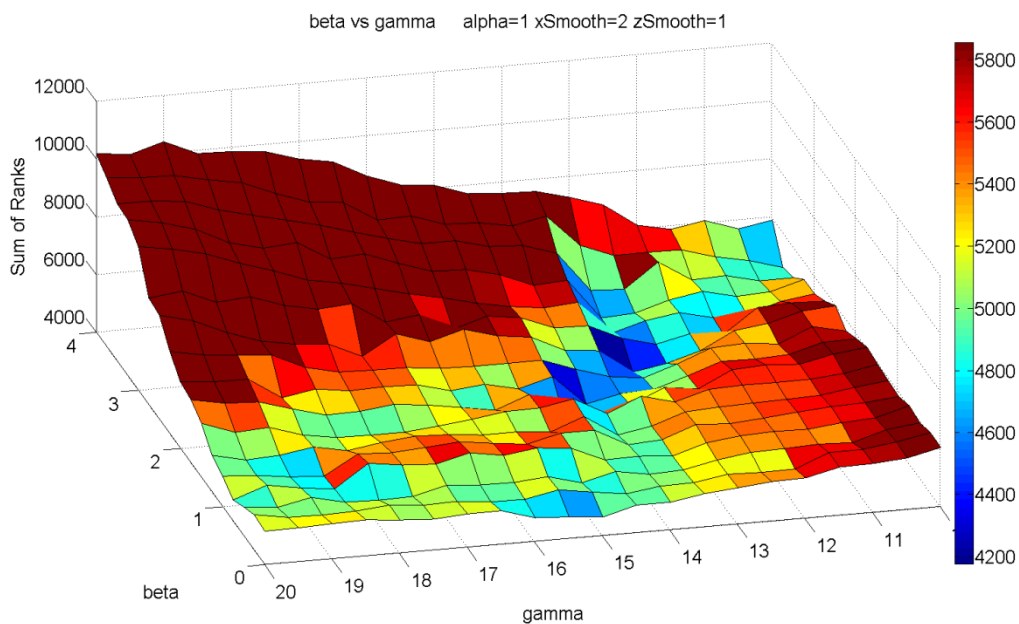

Figure 31. A surface plot of the error space when beta and gamma are changing and alpha, xSmooth and zSmooth are held constant. Alpha is 1, xSmooth is 2 and zSmooth is 1.

Due to the roughness of the surfaces in the previous figures, the optimization process was halted at this scale. Figure 30 has the most dark blue squares in the surface. This means that the parameter sets with alpha at 0.95 have the best chance to lead to accurate measurements. Even though the best parameter set from Table 2 had a beta of 1.75 and a gamma of 15, a beta of 2.25 and a gamma of 13.5 leaves some room for error. The centroid of the dark blue area in Figure 30 is approximately at a beta of 2.25 and gamma of 13.5. The best parameter set for this group of patient data is:

Alpha: 0.95

Beta: 2.25

Gamma: 13.5

xSmooth: 2

zSmooth: 1

3.2 Estimation of Error

To estimate the error for a new case the optimization process described in the previous section was performed on 5 of the 6 cases and the best parameter set was used to test the final case. This was repeated leaving a different case out each time. The parameter sets were chosen from the lowest sum of ranks in a broad global search, similar to Table 1 when all of the patients were used. There was no specific search for the error estimation. Table 3 shows the optimal parameter sets depending on which patient's dataset is left out. The error of the 6 tests is reported below in Figure 32. The error is the average absolute difference in cross-sectional area across all slices in units of mm². Table 4 shows the error transformed to equivalent radial error by taking the square root of the original error divided by pi. It also shows how the error compares to the size of the airway and the spacing of voxels in the image.

Table 3. The best parameter set after optimizing without one of the data sets.

Left-Out	alpha	beta	gamma	xSmooth	zSmooth
Patient 1	0.8	4	8	3	1
Patient 2	0.8	2	14	2	1
Patient 3	0.8	0	16	3	1
Patient 4	0.8	2	14	2	1
Patient 5	1	0	20	1	1
Patient 6	0.8	0	30	3	1

The first parameter set is if the optimization is done
without patient 1. The second is if the optimization is
performed without patient 2 etc.
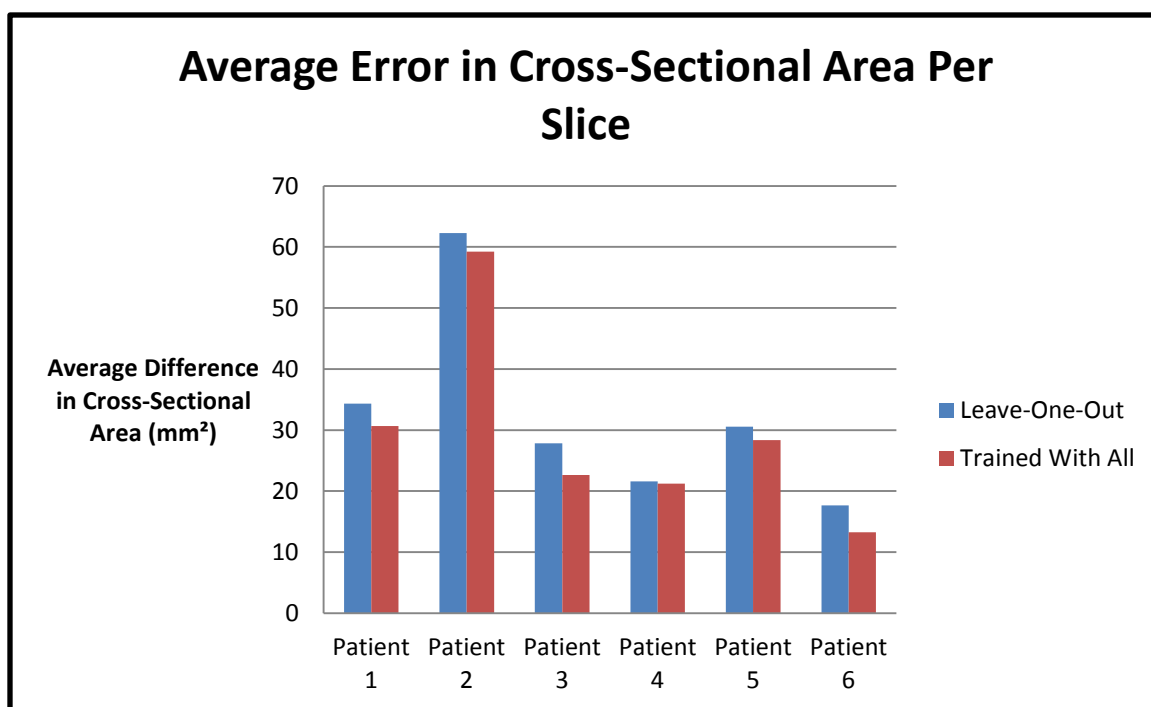
Figure 32. Blue – Average error in cross-sectional area from testing with the patient after
optimizing the parameters (training) using the other five patients. Red –
Average error in cross-sectional area after training with all six cases.

Table 4. Shows the error results with respect to other image and airway metrics.

Left-Out	Equivalent Diameter Error (mm)	Cross-Sectional Area Error (mm²)	Average Cross-Sectional Area (mm²)	Error as % of the Average Cross-Sectional Area (%)	Voxel Spacing X,Y,Z (mm)
Patient 1	6.61	34.34	240.66	14.27	0.86,0.86,5
Patient 2	8.90	62.28	238.32	26.13	0.86,0.86,6
Patient 3	5.95	27.82	176.22	15.79	0.86,0.86,5
Patient 4	5.25	21.61	115.46	18.72	0.78,0.78,5
Patient 5	6.24	30.57	240.70	12.70	0.86,0.86,6
Patient 6	4.74	17.68	137.56	12.85	0.70,0.70,6
MEAN	6.28	32.38	191.49	16.74	0.82,0.82,5.5

The average error for the 6 tests was 32.38mm². In figures 32 through 35, the measurements obtained for Patient 5's MR image have been plotted against Pulmonary Workstation's measurements of the CT data. Two parameter sets were used to measure the image. They were the optimal sets found from training with and without patient 5. Figure 36 shows the optimal surface converted back to the original image domain and overlaid on the registered MR and CT images.
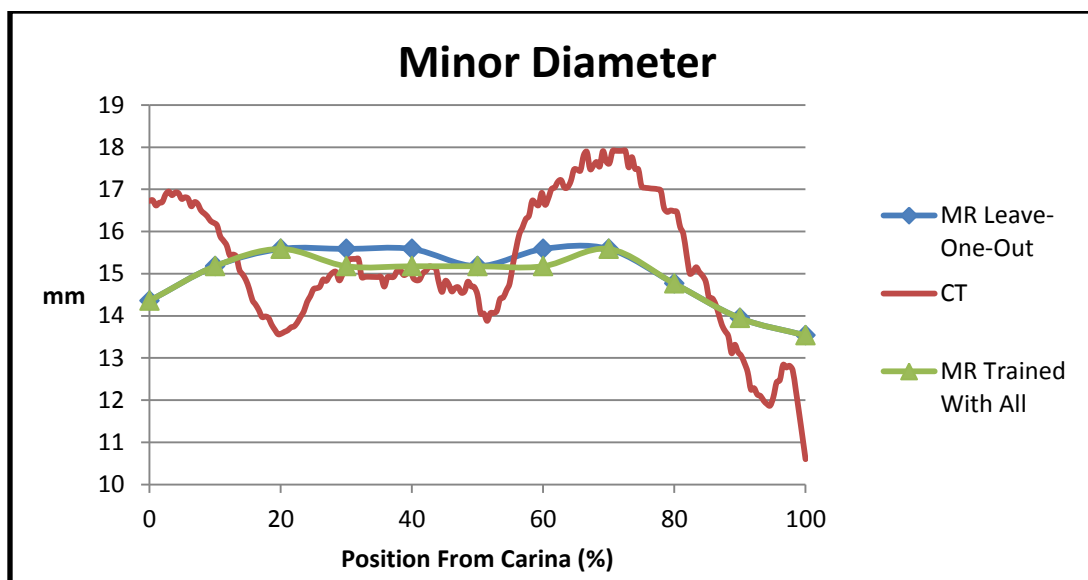
Figure 33. Comparison between the minor diameters measured from the MR image and CT image (Pulmonary Workstation, red) of Patient 5 after obtaining the optimal parameter set with the other five patients (blue) and with Patient 5 included in the optimization (green).
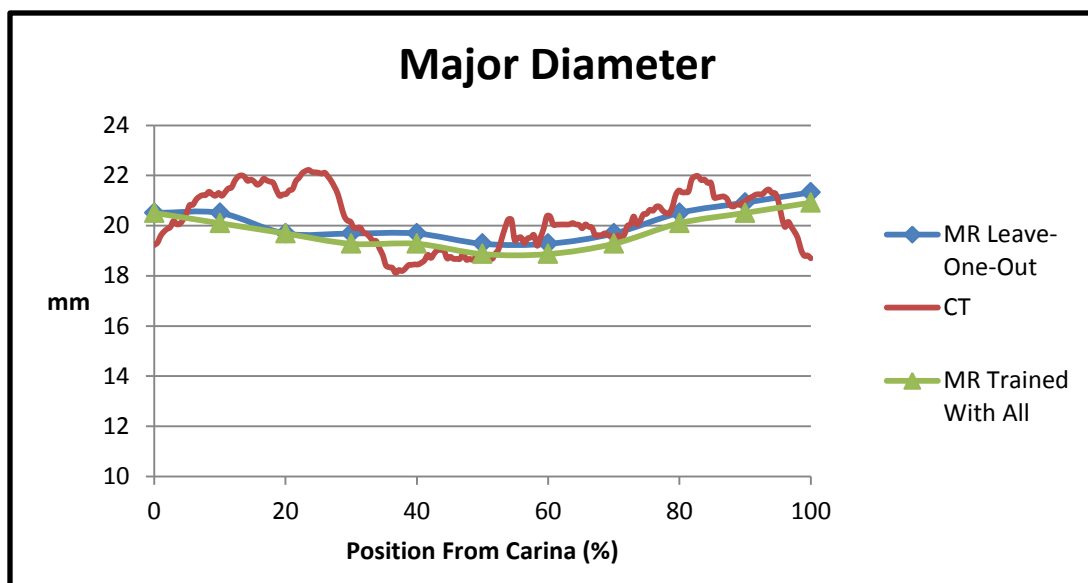
Figure 34. Comparison between the major diameters measured from the MR image and CT image (Pulmonary Workstation, red) of Patient 5 after obtaining the optimal parameter set with the other five patients (blue) and with Patient 5 included in the optimization (green).
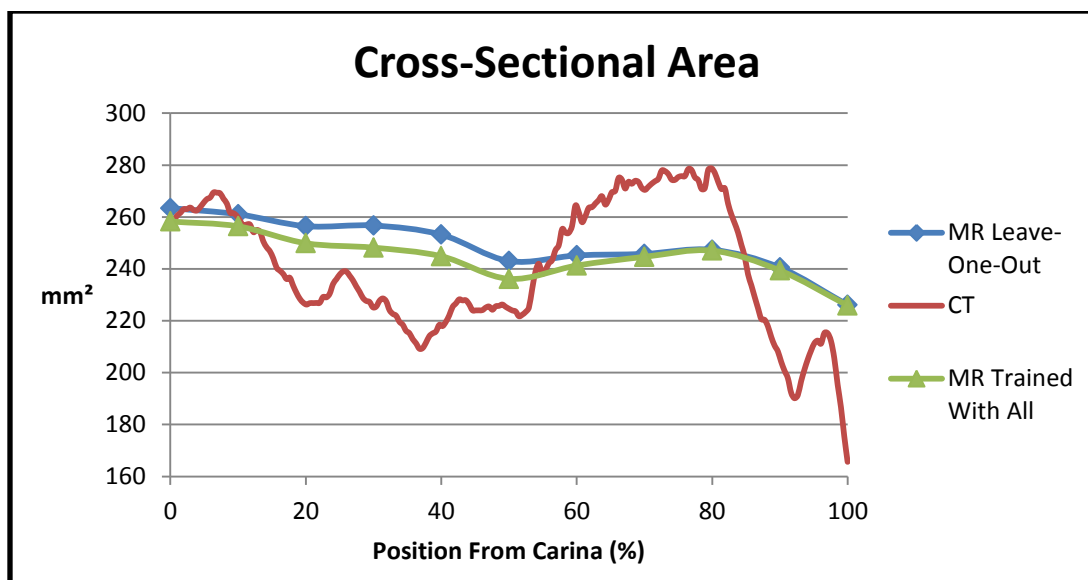
Figure 35. Comparison between the cross-sectional area measured from the MR image and CT image (Pulmonary Workstation, red) of Patient 5 after obtaining the optimal parameter set with the other five patients (blue) and with Patient 5 included in the optimization (green).
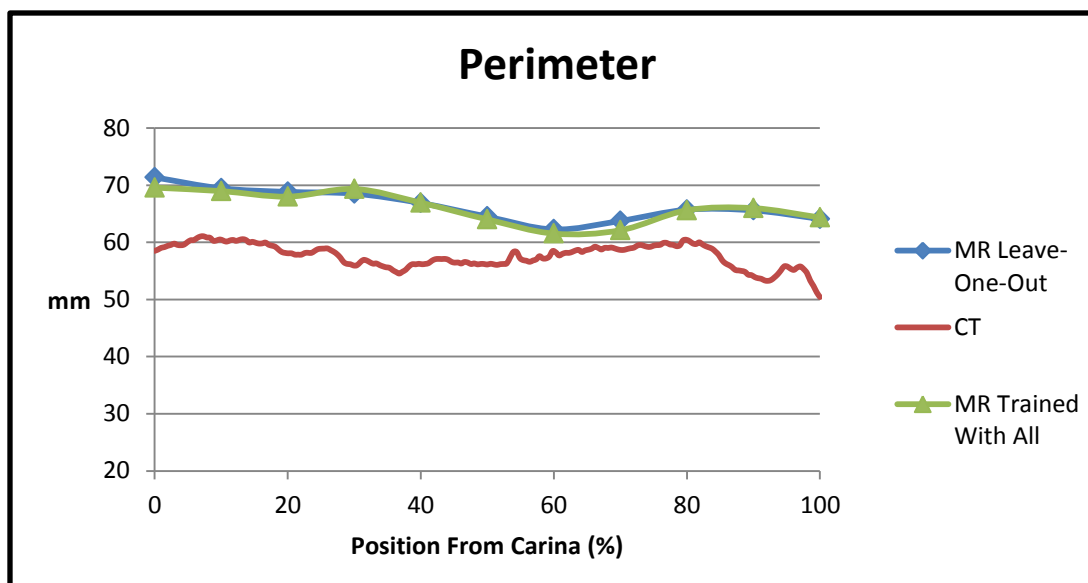
Figure 36. Comparison between the perimeters measured from the MR image and CT image (Pulmonary Workstation, red) of Patient 5 after obtaining the optimal parameter set with the other five patients (blue) and with Patient 5 included in the optimization (green).
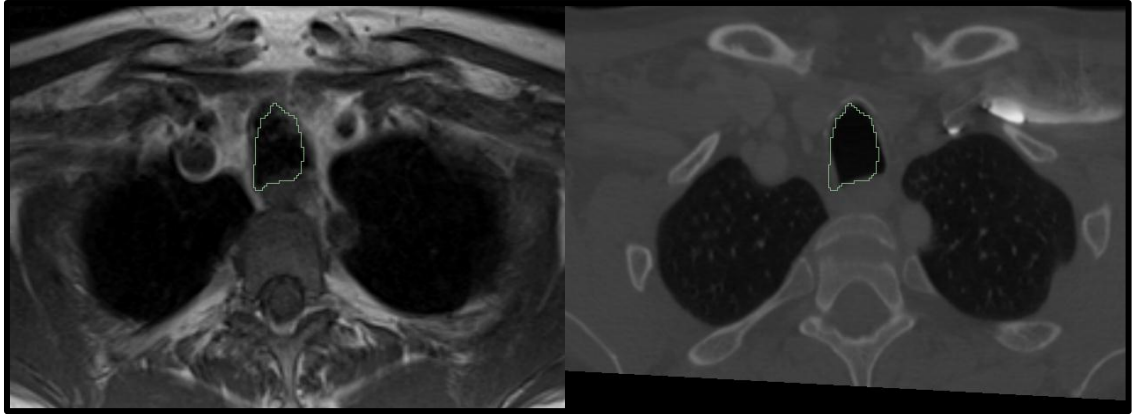
Figure 37. Example axial slice of an MR segmentation. The outline of the segmentation is overlayed on the MR (left) and CT (right) image that was rigidly registered to the MR data.

3.3 Measuring Pediatric Population

Using the best parameters from the optimization with all 6 cases, a pediatric population was measured. The demographics of the population are shown below in Table 4 as well as a histogram of the age distribution in Figure 38.

Table 5. Pediatric Patient Demographics

Patient	Sex	ID Number	Age	Weight(kg)	Height(cm)	BMI
1	male	66	1.58	11.8	83	17.13
2	male	27	2.46	15.5	94	17.54
3	male	38	3.4	16.3	96.6	17.47
4	male	63	3.5	14	91.5	16.72
5	male	67	3.6	15.2	97	16.15
6	female	24	4	14.515	107.3	12.61
7	male	69	4.5	19.1	117	13.95
8	female	47	5.1	16.7	105	15.15
9	female	44	7.77	34.519	125	22.09
10	female	30	8	15.874	114.8	12.04
11	male	26	9.49	23.2	125.5	14.73
12	male	25	10	36.228	128	22.11
13	female	51	10.8	28.5	125	18.24
14	male	28	10.93	54.885	141.8	27.30
15	male	31	11	51.2	152.8	21.93
16	female	43	11.8	37.9	150.3	16.78
17	male	34	12.2	43	148.4	19.53
18	male	75	12.67	56.2	161.7	21.49
19	male	29	13	70.8	158	28.36
20	male	42	13.7	54.7	164.3	20.26
21	female	59	14.4	50.89	160	19.88
22	male	68	15.9	82.6	185.4	24.03
23	male	35	16.8	52.3	164.7	19.28
24	female	58	17	52.7	154.9	21.96
25	female	33	18	57.5	167.6	20.47

The ID Number is a deindentification number

Age Histogram
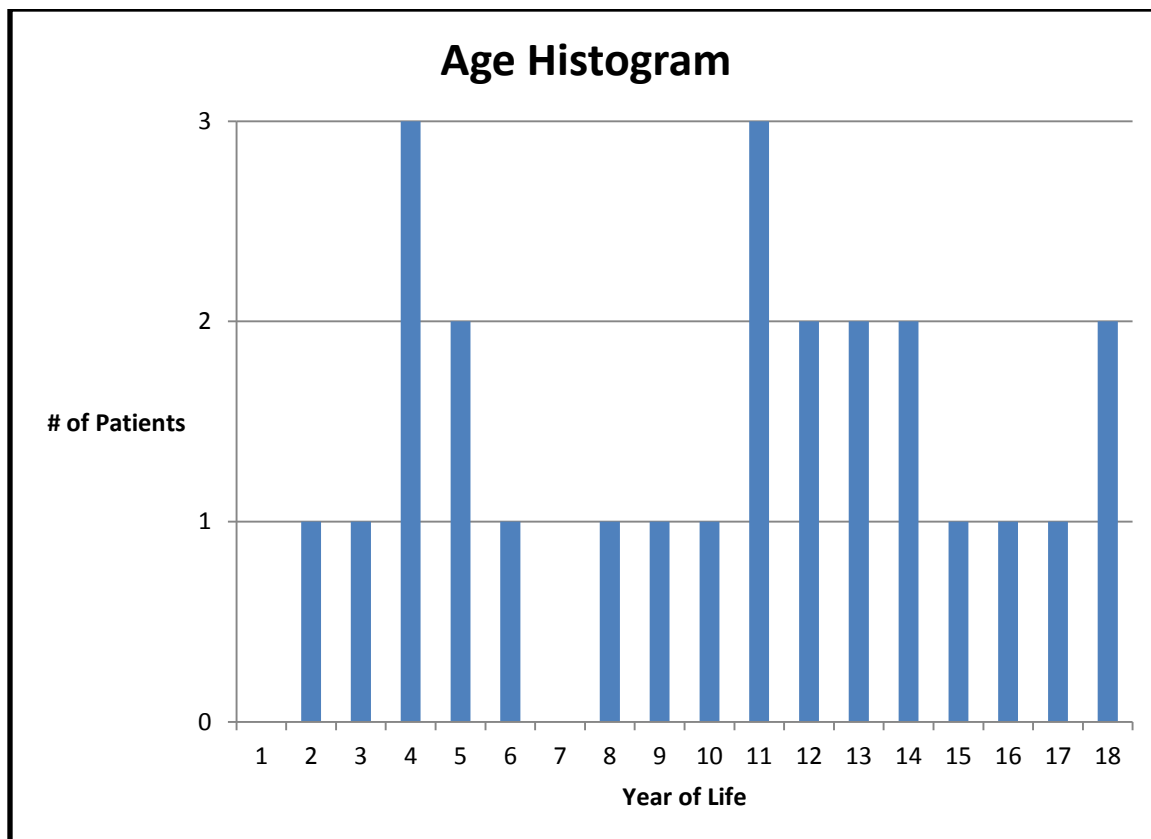
Figure 38. Distribution of age in the pediatric population tested

The cross-sectional areas are plotted versus age, height, weight and BMI in figures 39 through 42. The average diameters are also plotted against age in figure 43. A second order polynomial is fit to each plot. Age and height show the best correlation with R^2 values ranging from 0.73 to 0.83. Using the residual error between the measurements and the 2nd degree polynomial fit to the data, a standard deviation was calculated and a 95% confidence interval was plotted with the best fit line. Figure 44 shows the cross-sectional area plotted against age with the 95% confidence interval.
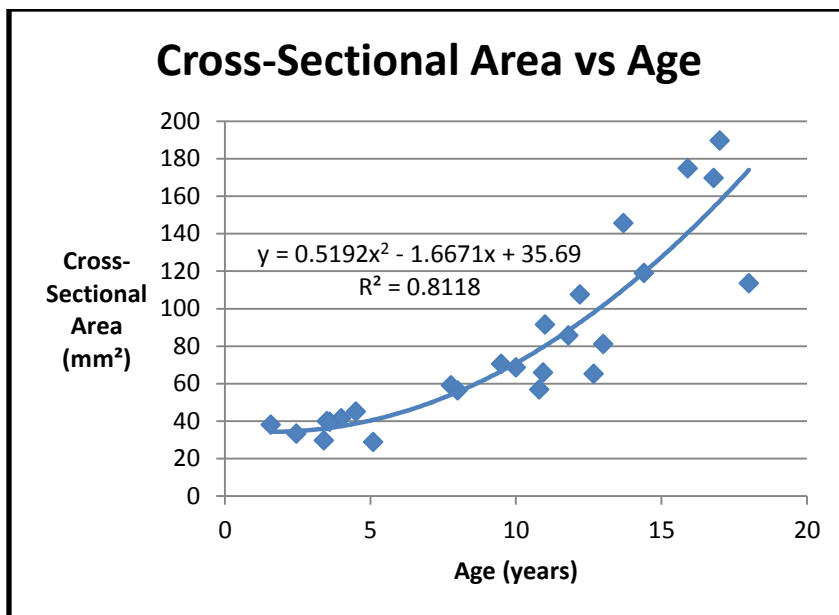
Figure 39. The average cross-sectional area for each child is plotted against their age. The trendline shown is a 2nd order polynomial.
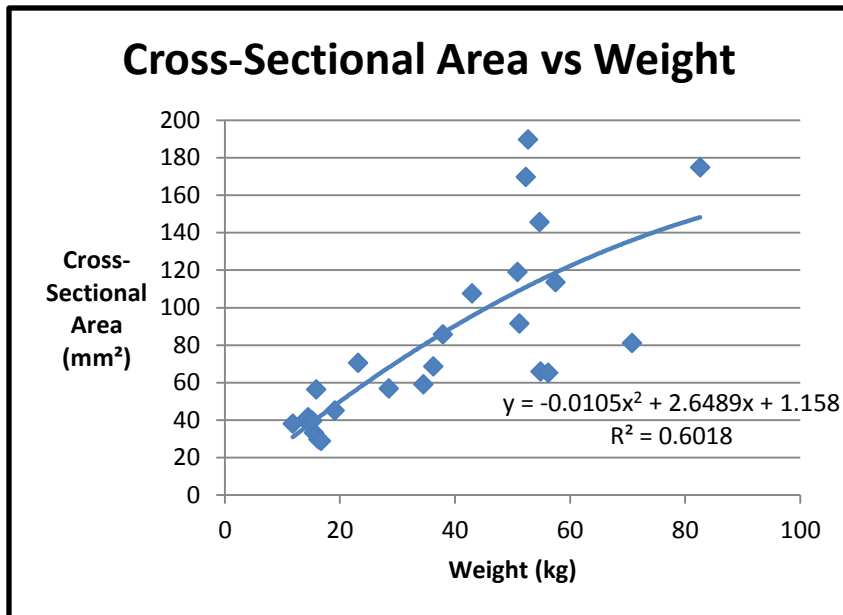
Figure 40. The average cross-sectional area for each child is plotted against their weight. The trendline shown is a 2nd order polynomial.
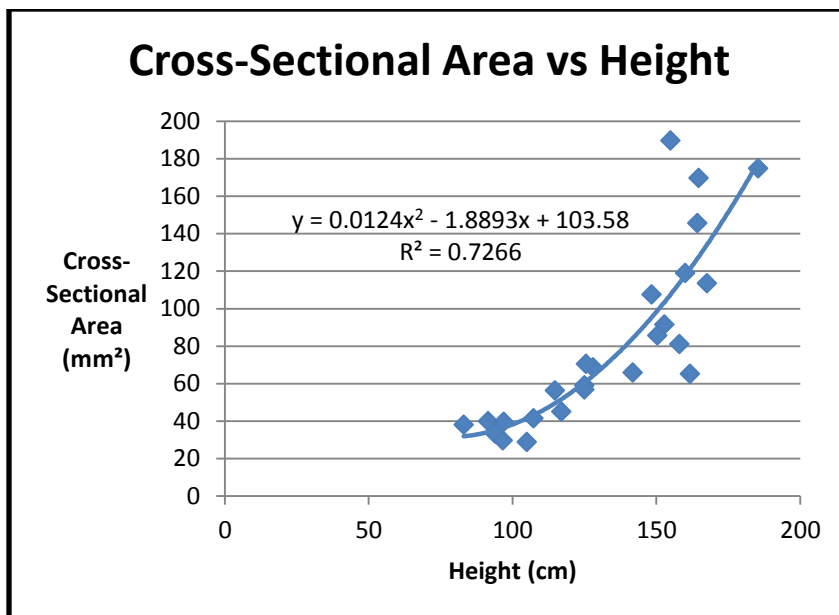
Figure 41. The average cross-sectional area for each child is plotted against their height. The trendline shown is a 2nd order polynomial.
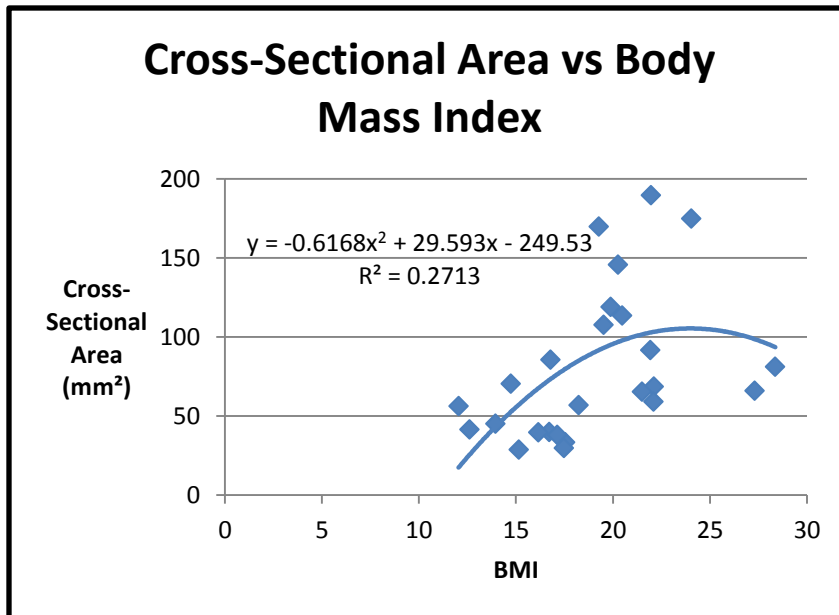
Figure 42. The average cross-sectional area for each child is plotted against their BMI. The trendline shown is a 2nd order polynomial.
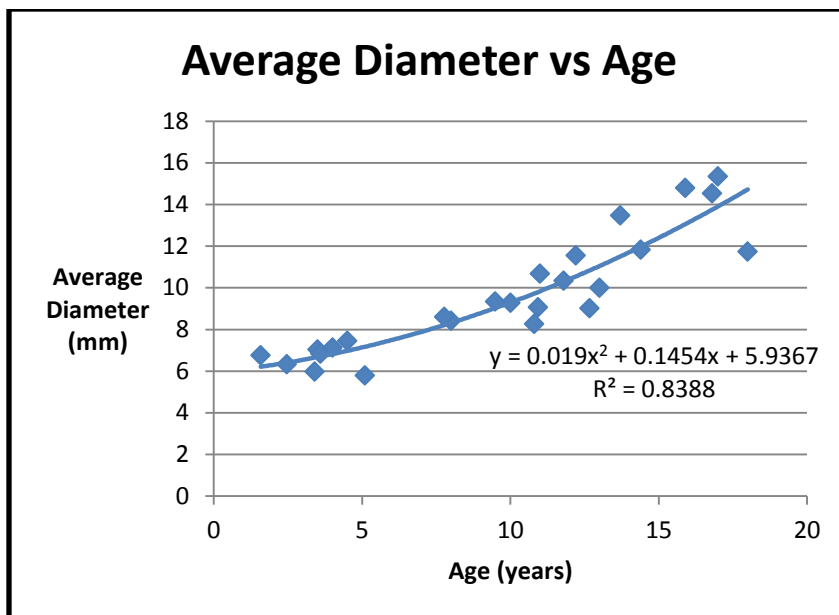
Figure 43. The average diameters for each child are plotted against their age. The trendline shown is a 2nd order polynomial.
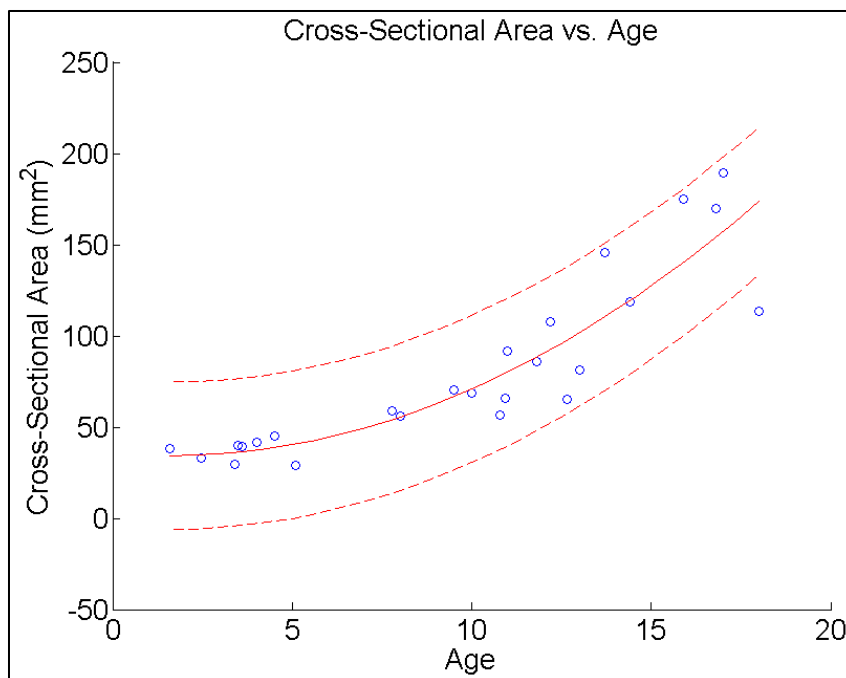
Figure 44. Cross-sectional area plotted against age. The upper and lower bounds show a 95% confidence interval (dashed) of the best fit line (solid).

After an expert manually segmented the trachea from five axial slices, the distance between closest boundary points of the manual and automatic segmentations are shown below. A boundary point was defined as a voxel of the segmentation that touches a background voxel using 4-connectivity. Figure 45 shows a histogram of the all the measurements and Figure 46 shows the median error for each of the 25 patients as well as the 1st and 3rd quartile and minimum and maximum error. Approximately 80% of the boundary points have an error of 1mm or less.
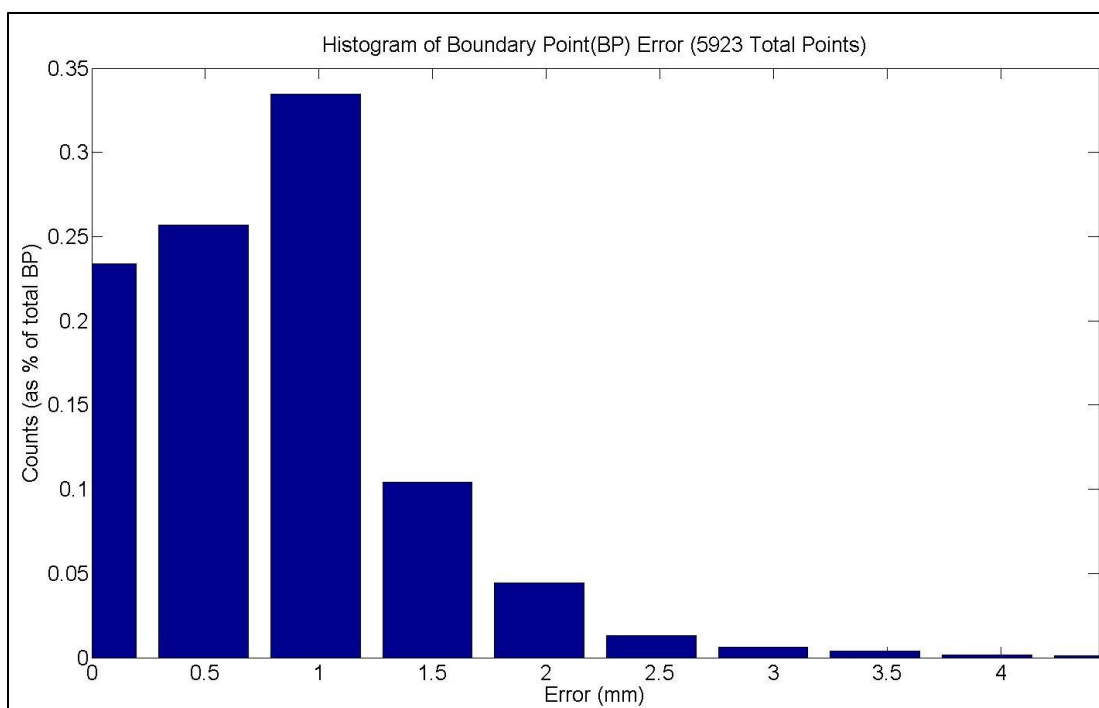
Figure 45. Histogram of the distance between all boundary points of the manual and automatic segmentations.
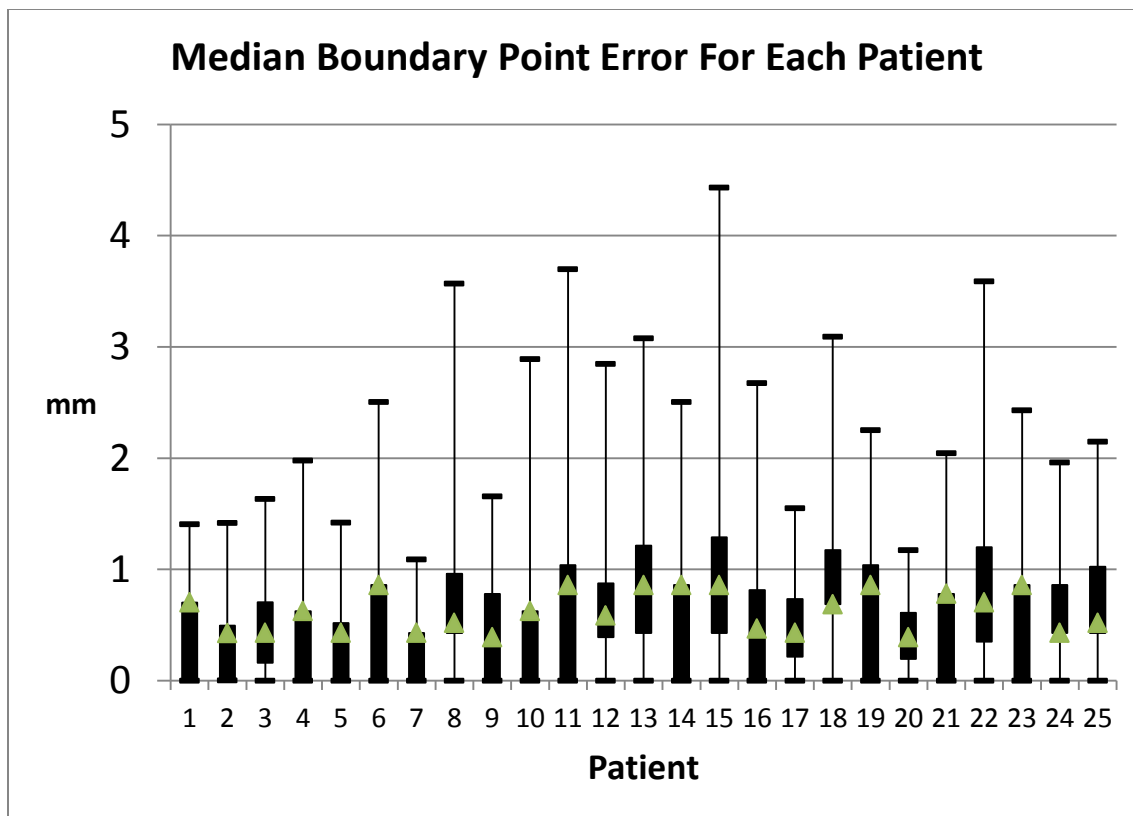
Figure 46. The median boundary point differences between the manual and automatic segmentations for each patient. The green triangle represents the median. The lower and upper limits of the black rectangle represent the 1st and 3rd quartile. The error bars show the minimum and maximum error.

CHAPTER 4

DISCUSSION

4.1 Parameter Optimization

The method of ranking the best parameter set is a point of discussion. It would be ideal if the actual error between the MR and CT cross-sectional areas could be used as the metric for ranking the best parameter sets. We did not believe this was the best approach because some patients had very large error compared to the others. This may have been because of the image quality or the size of the airway. Also, each patient had different amount of overlapping CT and MR data. To normalize the effect that each patient has on the ranking of the parameter sets, each set was given a separate ranking for each patient and the rankings were added together.

Figures 20, 21 and 22 show the effects of changing xSmooth from 1 to 3. The differences are not extremely obvious, but when xSmooth is 1, the surface does not reach the dark blue. When xSmooth is 2 or 3 the surfaces are very similar and both reach the dark blue. When xSmooth is 2, the surface does not rise up to a high error as quickly as when xSmooth is 3. Figures 21 and 24 depict the effects of changing zSmooth from 1 to 2. There is an obvious advantage having zSmooth at 1. Figures 21, 24 and 25 show the effects of lowering alpha from 1 to 0.8 to 0.6. The dark blue minimum is slightly greater when alpha is 1.

After a more specific examination of the error space corresponding to the pink square in figure 21, the optimization process was able to determine a parameter set to perform measurements on the pediatric population. It is encouraging that the parameter combinations surrounding the parameter set of alpha at 0.95, beta at 2.25, gamma at 13.5, xSmooth at 2 and zSmooth at 1 also produce similar results.

Eventually, when more images of the same type are collected or prospective images are acquired for quality, this is a parameter optimization process that can be applied easily to a new or larger population.

4.2 <u>Sensitivity</u>

The error estimation also produced reasonably good results. Table 3 shows the different parameter sets that are produced by leaving each patient out and optimizing based on the other five. All of the parameters stay relatively close, indifferent of the training set. Alpha is high, beta is low, and gamma is in the middle of the values tested. The average error across the test cases was approximately 32.38mm², shown in Figure 32. The equivalent average linear error was 6.28mm. There are many reasons for this significant of an error. First of all, the measurements of the CT scan produced by Pulmonary Workstation have an associated error. The measurement technique implemented in Pulmonary Workstation is described by Tschirren et al and shows that airways measured from an image with 0.361x0.361x0.6mm³ voxel size can expect a 0.26mm error. [39] The CT images used in this validation had approximately the same voxel size ranging from 0.36-0.56mm in the x and y directions and 0.3mm in the z direction.

Secondly, there is some error introduced when the CT scan and the MR image are registered. Although, in most cases the registration is good, when viewed by the naked eye, there must be a millimeter or two (at least) of error associated with the images not lining up.

Finally, the spacing of the voxels in the MR images of the adult validation cases averages 0.82x0.82x5.5mm³ as shown in Table 4. Since the diameter of the airway for these adults ranges from 13-20mm, 5.5mm is a significant percentage of the size of the airway and must play a role in how accurate this measurement technique can be.

It is also encouraging that in Figure 32 all of the red bars are smaller than the blue bars. That means that the error decreases in all cases when that patient is included in the training. Hopefully, if more patients were included in the validation the error will keep decreasing. Overall, the equivalent linear error of 6.28mm is pretty good accuracy considering the limitations mentioned above. Using patient 5 as an example, in Figures

33 through 36 it can be seen that if the CT data was severely smoothed it would resemble the MR measurements. Figure 37 shows that the segmentation produced from the MR image has a similar cross-sectional area as the airway in the CT image. The reason it is not completely overlaid on the CT airway may be due to initial registration.

One of the validation cases, patient 2, had extremely bad results when compared to the others. Further investigation into this issue showed that the segmentation of the MR image, shown in Figure 47, seemed reasonable. A possible contributing factor for this high error is depicted in Figure 48. Patient 2's trachea tends to move more in the anterior to posterior direction than the others. This means that when the image is resampled in planes normal to the centerline of the trachea, it is using more of the data from the sparsely sample axis than the densely sampled axes.
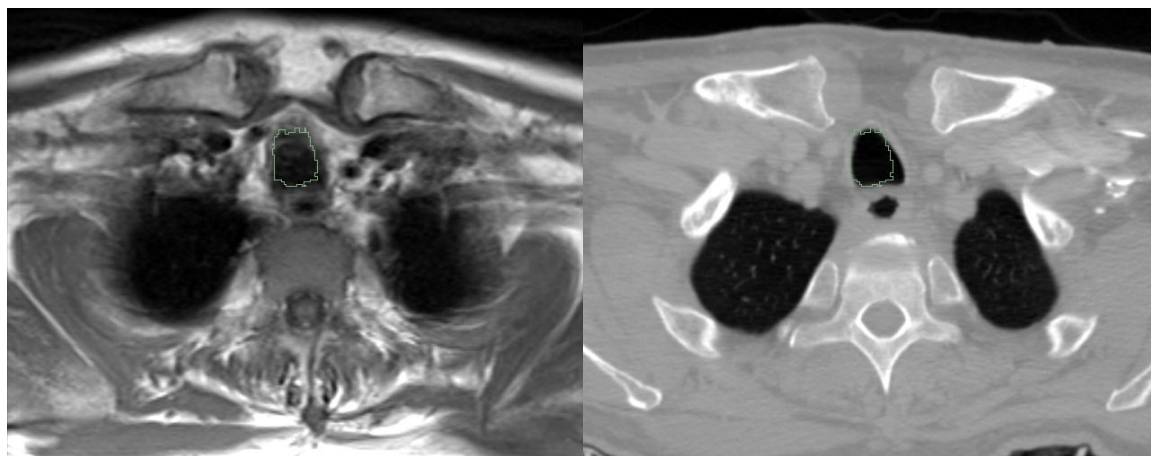
Figure 47. Segmentation of Patient 2 overlaid on the axial slices in MR (left) and CT (right) images.
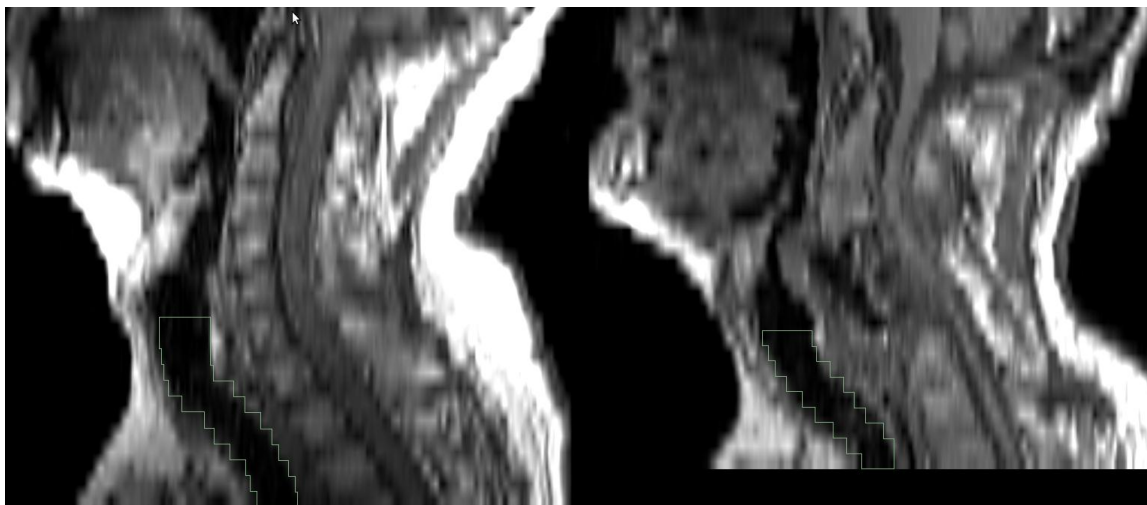
Figure 48. Sagittal view of two patient's MR segmentations. Patient 5's (left) trachea is more vertical than Patient 2's (right) trachea.

4.3 Error between Manual and Automatic Segmentations

When an expert in the field segmented some axial slices manually, there was error observed in closest boundary points. Figure 45 shows that approximately 80% of all boundary points of the manual segmentations were 1mm or less from the closest corresponding boundary point on the automatic segmentation. As shown in Figure 46, no patient displayed an extreme amount of error. In only six patients was the 3rd quartile above 1mm. All patients' 3rd quartile was less than 1.5mm. There are many possible reasons for this error. Most importantly, is the low resolution of the pediatric MR Images. The spacing in the transverse plane ranges from 0.5-1mm and from 3-6mm in the axial direction. That means that if closest boundary points are adjacent voxels, it could be up to 1mm error. Another reason for the error between the manual and automatic segmentations could be due to the fact that the program was optimized to produce similar results as measurements from a CT scan. The two imaging modalities measure different characteristics of the tissue that could lead to the expert actually measuring something different than is measured from the CT scan. For example, in a T1 relaxation MR

acquisition fluid and air both appear dark. This means the mucosal lining may not be detected in the MR image but would be detected in the CT scan.

4.4 Comparison to Previous CT Study

When a pediatric population was measured, cross-sectional area correlated very well with age and height. The size of their airway seemed to increase at an increasing rate when compared with the demographics so the data was fit to a 2nd order polynomial. The R^2 values for age and height vs. cross-sectional area were 0.81 and 0.73 respectively. Cross-sectional area did not correlate very well with weight and BMI. The R^2 values were 0.6 and 0.27 respectively. Initially, it was thought that all four of the demographics would correlate well with airway cross-sectional area. The reason that weight and BMI do not correlate very well may be because the population tested was not actually normal. All of the images were obtained by children that were in the hospital for a medical issue.
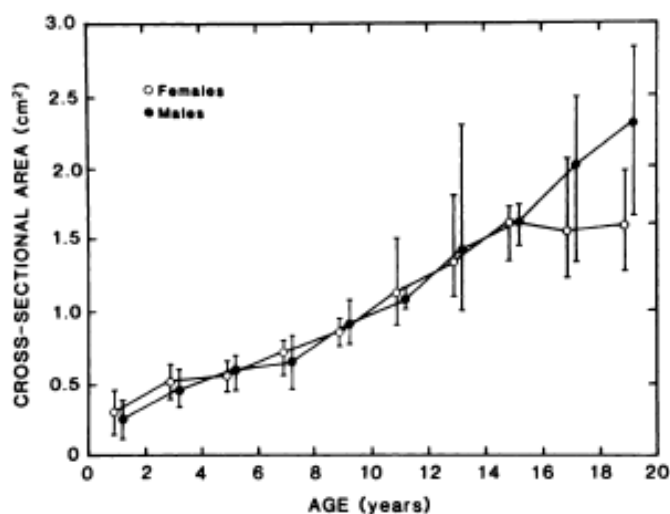
Figure 49. Cross-Sectional Area vs Age in Males and Females [38]

They may have had intravenous fluid or diarrhea at the time their weight measurement was taken. Something like this would skew any correlation. Age and height are not affected by any medication or illness.

Comparing figures 39 and 43 to figures 49 and 50 respectively from a previous study performed 20 years ago using CT images to attain measurements of the pediatric trachea, there are similarities. The lowest and highest values for cross-sectional area in both measurements are around 40 and 200 mm² respectively. Likewise for the diameters, the youngest children have diameters of about 5mm and the oldest children have diameters around 15mm. The data points from the CT study were extracted and plotted with our data in figures 51 and 52. There are similar trends, but the CT measurements are larger by approximately 0.1-0.2cm² and 0.1cm for cross-sectional area and diameter measurements respectively. This could to be attributed to the much lower resolution in the MR images. It also could be attributed to the fact that the program is optimized to produce good results for the adult airway. The parameters may have to be tweaked for optimal results in a pediatric population.
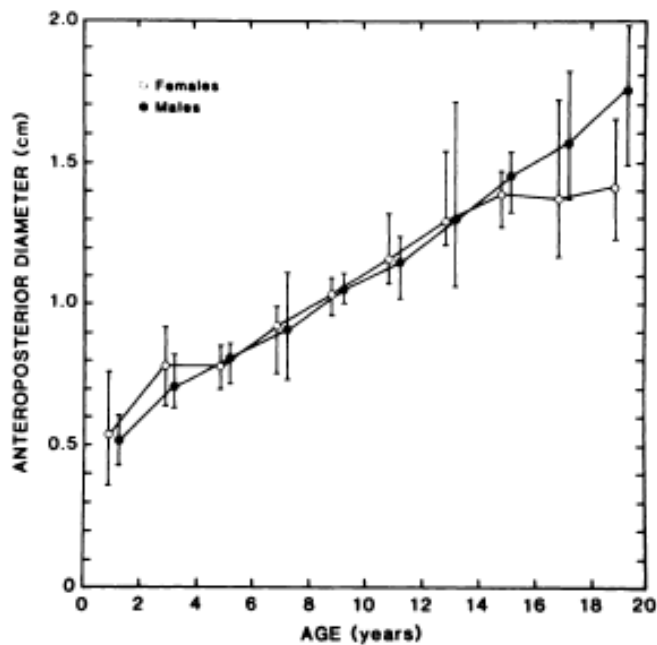
Figure 50. Anteroposterior Diameter vs Age in Males and Females [38]
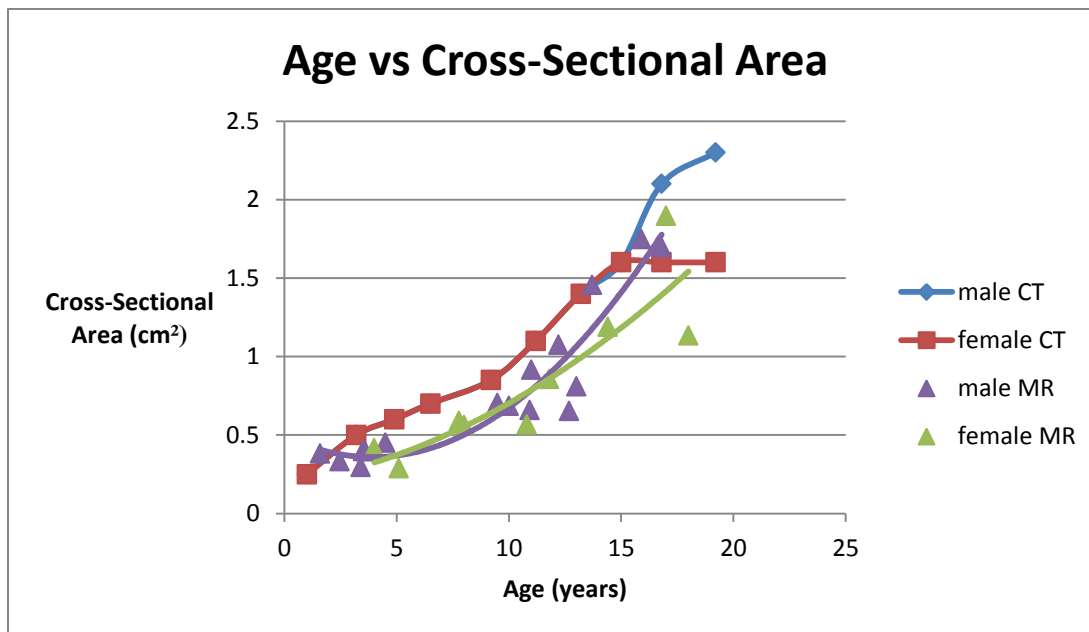
Figure 51. Figures 39 and 49 combined. Purple and Green triangles represent measurements from MR images. Red and Blue are the measurements from CT images.
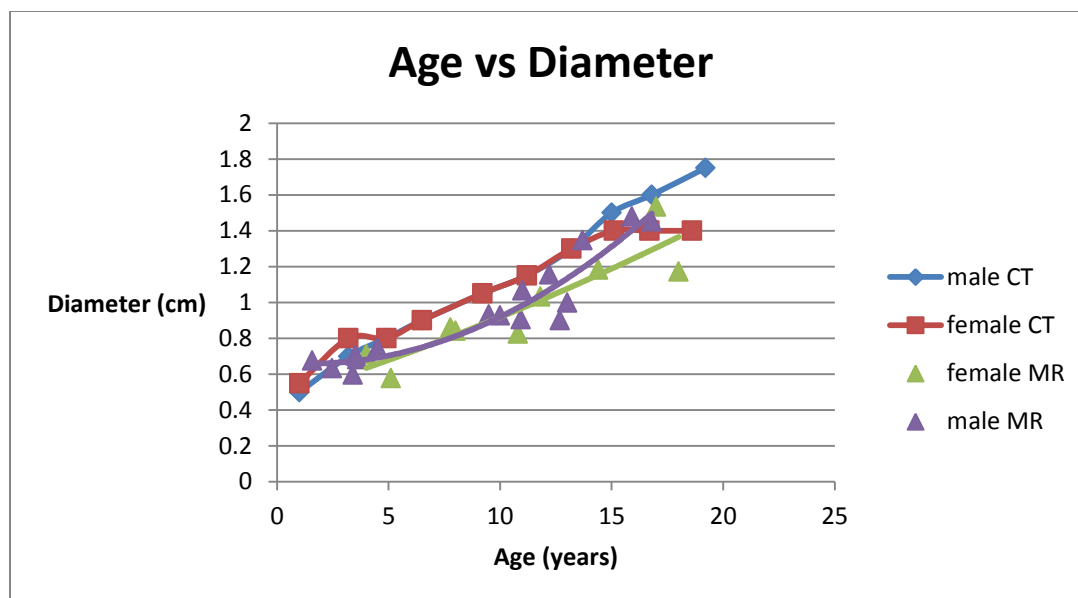
Figure 52. Figures 43 and 50 combined. Purple and Green triangles represent measurements from MR images. Red and Blue are the measurements from CT images.

4.5 <u>Limitations</u>

There are some limitations to the program. The MR images collected of very young children (<1 yrs) were not able to be analyzed. The spacing between axial slices was too great compared to the size of the airway. This leads to the airway being disconnected between every slice.

When comparing the CT and MR perimeter measurements for the adult cases, the perimeter measurement from the MR image is always greater than that of the CT image measured with Pulmonary Workstation. This is even after the extra smoothing is applied to the surface (described in 2.2.6) before the perimeter calculation is made.

If we were to do this study again, it would have been ideal to request IRB approval to look at the patients' reasons for hospitalization. This may give insight as to why our measurements deviate from the previous study using CT images and why weight and BMI do not correlate very well with cross-sectional area.

CHAPTER 5

SUMMARY AND FUTURE WORK

The overarching goal of this research is to develop a tool that can assist in establishing the characteristics of the normal airway and congenital abnormalities. This would greatly enhance a physician's ability to quantitatively assess if a reconstructed airway is enlarged enough to provide sufficient airflow. It could also assist in pre-surgical planning by better preparing the surgeon and lessening the time the patient is on cardio-pulmonary bypass. After reconstruction, this program could be used to monitor the growth of the reconstructed airway and how it compares to the growth of a normal child's airway.

The work in this thesis has described a tool that has the potential to accurately measure the pediatric trachea. Using an initial region growing to find the centerline of the trachea, the program used 1st and 2nd derivative information along with grayscale and position characteristics to locate an optimal surface for the airway. A process has also been outlined to optimize the software to produce expected results new groups of patients.

Even though all of the MR images found for validation of this program were originally obtained for clinical use only, the program was able to show trends in the growth of the pediatric trachea. If a prospective study was performed and images were acquired for quality, this program would be much more effective. Eventually, if images with higher resolution are acquired, more detailed measurements will need to be taken. As shown in Figure 53, Murgu and Colt reported that the airway can take many different shapes in when one of these tracheal anomalies are present. Simple major and minor diameter, cross-sectional area and perimeter would not be able to describe these types of shapes. Measures such as curvature, eccentricity, convexity and concavity will have to be investigated.
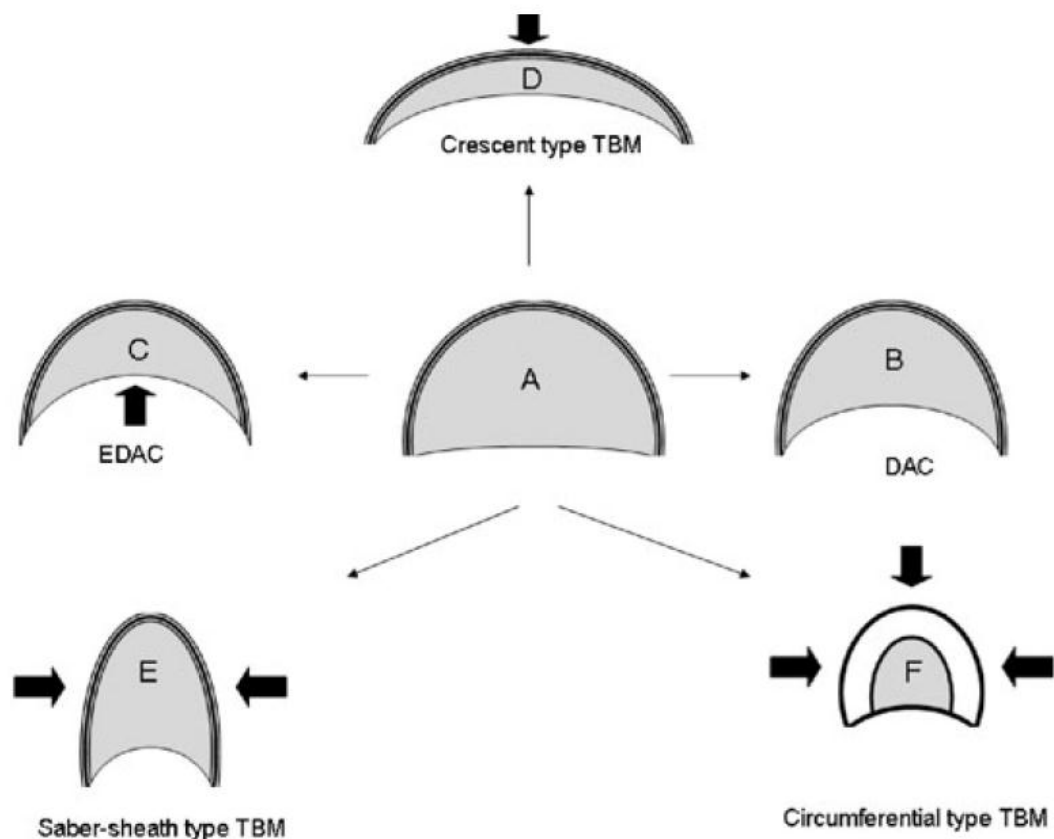
Figure 53. Airway lumen during inspiration (A). During expiration there is inward bulging of the posterior membrane. This process is physiological and is called dynamic airway collapse (DAC) (B). The pathologic exaggeration of this process results in a reduction in cross sectional area of 50% or more and is called excessive dynamic airway collapse (EDAC) (C). The pathological collapse of the cartilaginous rings represents tracheobronchomalacia (TBM). The crescent type TBM occurs when the anterior cartilaginous wall is softened and results in excessive narrowing of the sagittal airway diameter (D).The saber-sheath type TBM is due to softening of the lateral walls and excessive narrowing of the transverse airway diameter (E). Circumferential (combined) type TBM is characterized by anterior and lateral airway walls collapse and is usually associated with airway wall inflammation (F). [50]

Future additions to the program could include a more sophisticated method of

initially locating the airway. If all of the images processed with this software were of the

same acquisition type, an automated protocol could be put in place instead of the current fiducial point selection. The data processed in this study was from many different types of clinical acquisitions so it made it difficult to regulate where the airway would be in the image. Other additions could also include a more consistent method of obtaining an initial segmentation. Although a simple region growing works well most of the time, it is prone to leaking.

Eventually, it will be necessary to optimize the cost function parameters for a pediatric population. While doing so, it may be beneficial to have flexibility in the parameters depending on the size of the airway. Using the initial region growing to estimate the size of the airway, the parameters could be a piece-wise function based off of size.

APPENDIX – INSTRUCTIONS FOR RUNNING SLICER MODULE

<u>Installation</u>

Version 3.6 of 3DSlicer and version 2.8 of CMake must be installed to compile the code. (more recent versions should work as well) The code consists of a source, header and xml file. Once compiled, there is an executable file and a shared library file. The shared library file needs to be copied to 3DSlicer's modules directory to be able to run it inside of 3DSlicer.

<u>Running Module</u>

1.   Add the MR data file

    a.   The data should be oriented so the x-y plane is the transverse plane

    b.   The z-axis origin should be at the bottom of the data set (the mouth should have a higher z-index than the lungs

2.   Select fiducial points to mark the vocal cords and carina (they should be 2 separate lists)

3.   Set the input image to the MR image

4.   Set the carina and vocal cords to their respective fiducial lists

5.   Run the program by selecting Apply

6.   Manipulate the parameters for the initial segmentation until and reasonable segmentation is obtained

7.   Measurement results are stored in results.txt in the directory that Slicer is being run from

REFERENCES

1. Zoumalan, R., J. Maddalozzo, and L.D. Holinger, *Etiology of Stridor in Infants.* Annals of Otology, Rhinology & Laryngology, 2007. **116**(5): p. 329-334.
2. Hartnick, C.J., C. Bissell, and S.K. Parsons, *The impact of pediatric tracheotomy on parental caregiver burden and health status.* Arch Otolaryngol Head Neck Surg, 2003. **129**(10): p. 1065-9.
3. Wootten, C.T., et al., *Tracheotomy in the first year of life: outcomes in term infants, the Vanderbilt experience.* Otolaryngol Head Neck Surg, 2006. **134**(3): p. 365-9.
4. Mahadevan, M., et al., *Pediatric tracheotomy: 17 year review.* Int J Pediatr Otorhinolaryngol, 2007. **71**(12): p. 1829-35.
5. Ozmen, S., O.A. Ozmen, and O.F. Unal, *Pediatric tracheotomies: a 37-year experience in 282 children.* Int J Pediatr Otorhinolaryngol, 2009. **73**(7): p. 959-61.
6. Hopkins, C., et al., *The impact of paediatric tracheostomy on both patient and parent.* Int J Pediatr Otorhinolaryngol, 2009. **73**(1): p. 15-20.
7. Atmaca, S., et al., *Pediatric tracheotomy: 3-year experience at a tertiary care center with 54 children.* Turk J Pediatr, 2011. **53**(5): p. 537-40.
8. Cunningham, M.J., et al., *Slide Tracheoplasty for Long-Segment Tracheal Stenosis.* Arch Otolaryngol Head Neck Surg, 1998. **124**(1): p. 98-103.
9. Airway Reconstruction, T., *Recent challenges in the management of congenital tracheal stenosis: an individualized approach.* J Pediatr Surg, 2005. **40**(5): p. 774-80.
10. Herrera, P., et al., *The current state of congenital tracheal stenosis.* Pediatr Surg Int, 2007. **23**(11): p. 1033-44.
11. Oshima, Y., et al., *Management of pulmonary artery sling associated with tracheal stenosis.* Ann Thorac Surg, 2008. **86**(4): p. 1334-8.
12. Lee, K.J., et al., *Aortopexy for tracheomalacia with dextrocardia, pulmonary artery sling, and congenital tracheal stenosis.* Ann Thorac Surg, 2009. **88**(4): p. 1345-8.
13. Wijeweera, O. and S.B. Ng, *Retrospective review of tracheoplasty for congenital tracheal stenosis.* Singapore Med J, 2011. **52**(10): p. 726-9.
14. Bajaj, Y., et al., *Laryngotracheal reconstruction and cricotracheal resection in children: Recent experience at Great Ormond Street Hospital.* Int J Pediatr Otorhinolaryngol, 2012.
15. Andrews, B.T., et al., *Technique, Utility, and Safety of Awake Tracheoplasty Using Combined Laser and Balloon Dilation.* The Laryngoscope, 2007. **117**(12): p. 2159-2162.
16. Warwick, M., *Anatomy of the larynx, trachea and bronchi.* Anaesthesia & Intensive Care Medicine, 2005. **6**(8): p. 253-255.
17. Minnich, D.J. and D.J. Mathisen, *Anatomy of the trachea, carina, and bronchi.* Thorac Surg Clin, 2007. **17**(4): p. 571-85.
18. Newell, R.L.M., *Anatomy of the post-laryngeal airways, lungs and diaphragm.* Surgery (Oxford), 2011. **29**(5): p. 199-203.
19. Pohunek, P., *Development, structure and function of the upper airways.* Paediatr Respir Rev, 2004. **5**(1): p. 2-8.
20. Schroeder, J.W., Jr, N.D. Bhandarkar, and L.D. Holinger, *Synchronous Airway Lesions and Outcomes in Infants With Severe Laryngomalacia Requiring Supraglottoplasty.* Arch Otolaryngol Head Neck Surg, 2009. **135**(7): p. 647-651.
21. Altman, K.W., R.F. Wetmore, and R.R. Marsh, *Congenital Airway Abnormalities in Patients Requiring Hospitalization.* Arch Otolaryngol Head Neck Surg, 1999. **125**(5): p. 525-528.

22. Olney, D.R., et al., *Laryngomalacia and Its Treatment.* The Laryngoscope, 1999. **109**(11): p. 1770-1775.
23. Richter, G.T. and D.M. Thompson, *The surgical management of laryngomalacia.* Otolaryngol Clin North Am, 2008. **41**(5): p. 837-64, vii.
24. Bath, A.P., et al., *Paediatric subglottic stenosis.* Clin Otolaryngol Allied Sci, 1999. **24**(2): p. 117-21.
25. *Functional Modeling of Pediatric Upper Airway Disorders (R01)*, D.o.H.a.H. Services, Editor.
26. Frush, D.P., L.F. Donnelly, and N.S. Rosen, *Computed tomography and radiation risks: what pediatric health care providers should know.* Pediatrics, 2003. **112**(4): p. 951-7.
27. Hawkins, D.B., *Glottic and subglottic stenosis from endotracheal intubation.* Laryngoscope, 1977. **87**(3): p. 339-46.
28. Dalal, P.G., et al., *Upper airway dimensions in children using rigid video-bronchoscopy and a computer software: description of a measurement technique.* Paediatr Anaesth, 2008. **18**(7): p. 645-53.
29. Jowett, N., et al., *Airway Luminal Diameter and Shape Measurement by Means of an Intraluminal Fiberoptic Probe: A Bench Model.* Arch Otolaryngol Head Neck Surg, 2008. **134**(6): p. 637-642.
30. Williamson, J.P., et al., *Measuring airway dimensions during bronchoscopy using anatomical optical coherence tomography.* European Respiratory Journal, 2010. **35**(1): p. 34-41.
31. Williamson, J.P., et al., *Quantifying tracheobronchial tree dimensions: methods, limitations and emerging techniques.* Eur Respir J, 2009. **34**(1): p. 42-55.
32. Dalal, P.G., et al., *Pediatric laryngeal dimensions: an age-based analysis.* Anesth Analg, 2009. **108**(5): p. 1475-9.
33. ARENS, R., et al., *Magnetic Resonance Imaging of the Upper Airway Structure of Children with Obstructive Sleep Apnea Syndrome.* Am J Respir Crit Care Med, 2001. **164**(4): p. 698-703.
34. Arens, R., et al., *Upper airway size analysis by magnetic resonance imaging of children with obstructive sleep apnea syndrome.* Am J Respir Crit Care Med, 2003. **167**(1): p. 65-70.
35. Tzeng, Y.S., et al., *Comparison of airway diameter measurements from an anthropomorphic airway tree phantom using hyperpolarized 3He MRI and high-resolution computed tomography.* Magn Reson Med, 2007. **58**(3): p. 636-42.
36. van Beek, E.J. and J.M. Wild, *Hyperpolarized 3-helium magnetic resonance imaging to probe lung function.* Proc Am Thorac Soc, 2005. **2**(6): p. 528-32, 510.
37. Wang, B., et al., *3D airway segmentation via hyperpolarized 3He gas MRI by using scale-based fuzzy connectedness.* Computerized Medical Imaging and Graphics, 2004. **28**(1-2): p. 77-86.
38. Griscom, N. and M. Wohl, *Dimensions of the growing trachea related to age and gender.* American Journal of Roentgenology, 1986. **146**(2): p. 233-237.
39. Tschirren, J., et al., *Intrathoracic airway trees: segmentation and airway morphology analysis from low-dose CT scans.* Medical Imaging, IEEE Transactions on, 2005. **24**(12): p. 1529-1539.
40. Liu, J., et al., *System for Upper Airway Segmentation and Measurement with MR Imaging and Fuzzy Connectedness.* Academic Radiology, 2003. **10**(1): p. 13-24.
41. Sonka, M., V. Hlavac, and R. Boyle, *Image processing, analysis, and machine vision.* 3rd ed. 2008, Toronto: Thompson Learning. xxv, 829 p.
42. Kang, L., *Optimal Surface Segmentation in Volumetric Images-A Graph-Theoretic Approach.* IEEE Transactions on Pattern Analysis and Machine Intelligence, 2006. **28**: p. 119-134.
43. Lemons, J.A., R.L. Schreiner, and E.L. Gresham, *Relationship of brain weight to head circumference in early infancy.* Hum Biol, 1981. **53**(3): p. 351-4.

44. Bartholomeusz, H.H., E. Courchesne, and C.M. Karns, *Relationship between head circumference and brain volume in healthy normal toddlers, children, and adults.* Neuropediatrics, 2002. **33**(5): p. 239-41.
45. Karvonen, M., et al., *New Finnish reference for head circumference from birth to 7 years.* Ann Med, 2011.
46. Dolk, H., *The predictive value of microcephaly during the first year of life for mental retardation at seven years.* Dev Med Child Neurol, 1991. **33**(11): p. 974-83.
47. Kuczmarski, R.J., et al., *2000 CDC Growth Charts for the United States: methods and development.* Vital Health Stat 11, 2002(246): p. 1-190.
48. Boykov, Y. and V. Kolmogorov, *An experimental comparison of min-cut/max-flow algorithms for energy minimization in vision.* Pattern Analysis and Machine Intelligence, IEEE Transactions on, 2004. **26**(9): p. 1124-1137.
49. Li, K., et al. *Efficient optimal surface detection: theory, implementation, and experimental validation.* 2004. SPIE.
50. Murgu, S.D. and H.G. Colt, *Tracheobronchomalacia and excessive dynamic airway collapse.* Respirology, 2006. **11**(4): p. 388-406.